Title
Atmospheric River Frequency-Category Characteristics Shape U.S. West Coast Runoff

Journal
Journal of Geophysical Research: Atmospheres, 130(2)

ISSN
2169-897X

Authors
Zhou, Yang
North, Joshua S
Rhoades, Alan M
et al.

Publication Date
2025-01-28

DOI
10.1029/2024jd041805

JGR Atmospheres

RESEARCH ARTICLE
10.1029/2024JD041805

Atmospheric River Frequency-Category Characteristics Shape U.S. West Coast Runoff

Yang Zhou[1], Joshua S. North[1], Alan M. Rhoades[1], Jing Tao[1], William Rudisill[1], Mark D. Risser[1], and William D. Collins[1,2]

[1]Lawrence Berkeley National Laboratory, Berkeley, CA, USA, [2]University of California, Berkeley, CA, USA

Key Points:

- High-category atmospheric rivers (ARs) and land preconditions significantly influence runoff response
- Weaker ARs can cause extreme runoff given saturated soil or high snowmelt
- Back-to-back ARs intensify runoff response and may increase flood risks

Supporting Information:

Supporting Information may be found in the online version of this article.

Correspondence to:

Y. Zhou,
yzhou2@lbl.gov

Citation:

Zhou, Y., North, J. S., Rhoades, A. M., Tao, J., Rudisill, W., Risser, M. D., & Collins, W. D. (2025). Atmospheric river frequency-category characteristics shape U.S. West Coast runoff. *Journal of Geophysical Research: Atmospheres*, *130*, e2024JD041805. https://doi.org/10.1029/2024JD041805

Received 13 JUN 2024
Accepted 24 DEC 2024

Author Contributions:

Conceptualization: Yang Zhou, Joshua S. North, Alan M. Rhoades, Jing Tao, William Rudisill, Mark D. Risser
Data curation: Yang Zhou, Alan M. Rhoades
Formal analysis: Yang Zhou, Joshua S. North
Funding acquisition: William D. Collins
Investigation: Yang Zhou, Alan M. Rhoades
Methodology: Yang Zhou, Joshua S. North, Alan M. Rhoades
Project administration: William D. Collins
Supervision: William D. Collins
Validation: Yang Zhou
Visualization: Yang Zhou, Joshua S. North, William Rudisill
Writing – original draft: Yang Zhou
Writing – review & editing: Yang Zhou, Joshua S. North, Alan M. Rhoades,

Abstract This study investigates the factors influencing runoff response to atmospheric rivers (ARs) over the U.S. West Coast. We focused on runoff time series variations impacted by AR characteristics (e.g., category and frequency) and land preconditions during Northern Hemisphere cool seasons in the period of 1940–2023. Results show that high-category ARs significantly increase local runoff with higher hourly precipitation rates leading to a greater incremental rate and peak runoff. Extreme runoff increases greatly with the AR category with an increase rate up to 12.5 times stronger than non-extreme runoff. Besides the AR category, land preconditions such as soil moisture and snowpack also play crucial roles in modulating runoff response. We found that runoff induced by weak-category ARs is more sensitive to land preconditions than high-category ARs, with high peak runoff occurring when soil is nearly saturated. Additionally, more than 50% of high-peak-runoff events in snow-covered grid cells are associated with rain-on-snow events particularly for the events associated with weaker ARs. Regression analysis reveals that AR precipitation and land preconditions jointly influence runoff, emphasizing the importance of including soil moisture and snowpack levels in AR impact assessments. The study also highlights the intensified runoff response to back-to-back ARs with short intervals, which may become more frequent with climate warming, posing increased flood risks via facilitating wet soil conditions. Our findings have significant implications for AR risk predictions and the development of prediction models for AR-induced runoff.

Plain Language Summary Atmospheric rivers are narrow bands of concentrated moisture in the atmosphere that can bring heavy rain when they reach land. Although it is known that stronger ARs carry more moisture and could lead to higher flood risk, the specific factors that influence these effects are not fully understood. For example, is a single strong AR as capable of producing flooding as a tightly sequenced set of less intense ARs, and how do antecedent land surface conditions (e.g., soil moisture and snowpack) attenuate or accentuate flood risk? This research investigates the relationship between AR characteristics, namely their intensity and landfall coupling frequency and the resulting runoff response on land at different AR landfall interval times and antecedent land surface conditions. We showed that weaker ARs can also cause significant runoff if they occur in conditions where the soil is already wet or the snow is ready to melt. Additionally, when ARs occur close together in time, the runoff from the second AR is often much higher because the land has not had enough time to release the water brought by the first one. This "back-to-back" effect is expected to become more common as the climate warms, potentially increasing flood risks.

1. Introduction

Atmospheric rivers are elongated corridors of intense moisture transport that play a crucial role in the hydrological cycle and are closely connected to extreme weather (Ralph et al., 2005; Zhu & Newell, 1998). Atmospheric rivers generally originate in tropical and subtropical regions and extend toward polar regions. Upon making landfall, ARs release large amounts of moisture as heavy precipitation due to frontal and orographic uplift (Rutz et al., 2014), leading to significant hydrological responses. Along the U.S. West Coast, ARs significantly contribute to precipitation and runoff, influencing regional water resources and flood risks (Dettinger et al., 2011; Konrad & Dettinger, 2017; Ralph & Dettinger, 2011; Ralph et al., 2006). Paltan et al. (2017) show that about 22% of total global runoff is attributed to ARs, and in California, ARs contribute between 20% and 50% of the state's annual precipitation and streamflow (Dettinger et al., 2011).

The hydrological impacts of a landfalling AR vary drastically depending on its intensity and duration (Ralph et al., 2019). Moderate ARs can act as drought busters, increasing water supply through landfall precipitation.

Jing Tao, William Rudisill, Mark D. Risser, William D. Collins

Approximately 30%–70% of persistent drought endings along the U.S. West Coast are associated with landfalling ARs (Dettinger, 2013). On the other hand, AR-associated extreme precipitation and strong winds during landfall often lead to hydrological extreme events (e.g., floods, flash floods, and landslides), posing additional risks to coastal urban areas (Chen et al., 2018; Hou & Chen, 2020; Lavers & Villarini, 2013; Ralph et al., 2006; Waliser & Guan, 2017). Additionally, studies focused on the U.S. West Coast have shown that higher temperatures at landfall can induce more rain-on-snow incidents, contributing to increased runoff (Chen et al., 2019; Rhoades et al., 2023). AR-associated precipitation events result in an almost doubling of the magnitude of runoff response compared to non-AR precipitation events (Siirila-Woodburn et al., 2023). Future warming scenarios project strengthened AR intensity, leading to more destructive land responses and increased economic losses (Corringham et al., 2022; Dominguez et al., 2018; Rhoades et al., 2020, 2021). Given the substantial role of ARs in local hydrology, advancing our understanding of how land-atmosphere interactions and their associated impacts vary with different AR characteristics is urgent for preventing hazards, mitigating risks, and establishing a resilient environment and infrastructure.

Antecedent soil moisture profoundly affects runoff generation and plays a crucial role in flood simulation and prediction (Hardie et al., 2011; Pathiraja et al., 2012; Tao & Barros, 2013; Tao et al., 2016; Wasko et al., 2020). Although runoff driven by extreme precipitation is less dependent on antecedent soil moisture (Wasko et al., 2020), decreasing soil moisture can offset future flood magnitudes, even though extreme precipitation is projected to increase (Sharma et al., 2018). Despite the direct impacts of landfalling ARs, pre-landfall land conditions (or preconditions), such as soil moisture and snowpack, influence the AR hydrological response. Only a handful of studies have specifically investigated changes in AR-related runoff responses under different land preconditions. For example, case studies have shown that the melting of antecedent snowpack caused by a category 4 AR significantly contributed to the extreme runoff at Oroville Dam in 2017 (Henn et al., 2020) and across northern California in 1997 (Rhoades et al., 2023). Higher runoff-to-precipitation ratios have been linked to antecedent soil moisture and existing snowpack (Leung & Qian, 2009), whereas low antecedent soil moisture has weakened the runoff response to a category 5 AR (Cao et al., 2019; Ralph et al., 2013). Additionally, the presence of snow potentially decreases the AR landfall temperature, which can influence the rate of snowmelt (Rudisill et al., 2021). Albano et al. (2020) analyzed the spatial variation of AR hydrologic impacts over the western U.S. in historical records and emphasized the important roles of water availability, temperature, and antecedent soil moisture in AR hydrologic responses. Recognizing the importance of land preconditions, Bowers et al. (2022) developed an AR flood risk model incorporating antecedent hydrological conditions. Prior to this study, Bowers et al. (2022) was the only one that included land preconditions in AR landfall impact assessments.

The impact of an AR event is not solely limited to AR intensity. Temporally consecutive back-to-back ARs can also significantly affect land surface hydrology, potentially strengthening the response to subsequent ARs. When multiple ARs make consecutive landfalls within a short period, high soil moisture from previous events increases the likelihood of flooding and landslides. Zhou et al. (2024) demonstrated that sequential ARs occurring within a short time could result in up to a 200% increase in runoff compared to ARs occurring further apart in time. During the 2017 Oroville Dam spillway incident, two back-to-back ARs with a 2-day interval contributed to extreme runoff with inflows from the second AR being approximately 46% stronger than those from the first (Henn et al., 2020). Using a water tracer model, H. Hu et al. (2018) showed that a large fraction of AR precipitation was retained in the soil for up to 6 months, indicating long-lasting impacts from ARs on surface hydrology. Within the context of increased AR frequency in future climates (Payne et al., 2020; Wang et al., 2023; Zhang et al., 2024), back-to-back AR occurrences are also projected to rise with rising temperatures and background moisture content (Bowers et al., 2023; Zhou et al., 2024). Therefore, understanding the relationship between runoff response, interval days between AR events, and AR categories is essential for prevention and mitigation actions regarding flooding and for building resilient environments and infrastructure.

Although existing research has highlighted the impacts of AR characteristics and land preconditions on runoff responses, significant gaps remain in understanding the complex interactions between these factors. For instance, although moderate ARs can alleviate drought conditions, the precise conditions under which weak ARs produce extreme runoff are still unclear. Moreover, the effects of back-to-back AR occurrences have not been thoroughly explored, particularly concerning their intensity and frequency. Although prior work has briefly discussed the response of runoff to back-to-back ARs (Zhou et al., 2024), this research builds on that foundation by delving deeper into the role of land preconditions and assessing the cumulative impacts of multiple consecutive ARs.

Given the substantial role of AR in local hydrology, it is urgent to advance our understanding of how land-atmosphere interactions and their associated impacts vary with different AR characteristics. Motivated by the need to understand the complex interactions between AR characteristics and their hydrological responses, this study aims to investigate the impacts of back-to-back AR events on runoff and assess the role of land preconditions, specifically soil moisture and snowpack, in modulating AR-induced runoff. Here, we will address two questions (a) How do AR intensity and frequency (i.e., the interval days between ARs) affect precipitation and the associated hydroclimate response over land? And (b) How do land preconditions impact the AR-related runoff response?

The paper is organized as follows. Section 2 introduces the data and methodology. Section 3 examines multiple variables that affect AR-induced runoff, including AR category, AR interval days, and land preconditions. In Section 4, we developed a regression model to estimate the overall runoff responses under different ARs and land conditions. We conducted a sensitivity test regarding AR detection uncertainty in Section 5. The summary and discussion are included in Section 6.

2. Data and Methodology

2.1. Reanalysis

We retrieved relevant variables from the fifth generation of the European Center for Medium-Range Weather Forecasts Reanalysis (ERA5) (Copernicus Climate Change Service, 2017; Hersbach et al., 2020). ERA5 provides high-resolution data with hourly intervals and a spatial resolution of 0.25° latitude by 0.25° longitude. In this study, we used 6-hourly time series, where the variables are 6-hourly averages. We focused on the cool season (September to March) from 1940 to 2023. We used integrated vapor transport (IVT), which is the vertical integration of moisture flux, to detect ARs. Additional relevant variables include runoff, volumetric soil moisture (VSM), 2 m temperature, and total precipitation. We obtained the VSM for four soil layers (0–7, 7–28, 28–100, and 100–289 cm) and then calculated the saturation degree for each layer by dividing the VSM by the porosity.

To identify the influence of snow conditions on runoff characteristics during AR events, we utilized ERA5 snow water equivalent (SWE) and snow depth to describe the lifecycles of the mass and energy of the snowpack. Snow water equivalent represents the depth of liquid water that would be produced by a snowpack if it were instantaneously melted. From an energy perspective, we used snow temperature across the five levels of the snowpack provided by ERA5 and calculated the cold content (CC) of the snowpack offline. The CC (MJ/m^2) is the vertical integral of snowpack internal energy, which shows the extent of energy needed for snowpack to melt. As described in Equation 6.27 of DeWalle and Rango (2008), CC is computed at each grid cell as

$$CC = c_i * \rho_s * h_s * (T_s - T_m)$$

where c_i is the specific heat of ice (0.00209 MJ/kg*K), ρ_s is the density of the snowpack (kg/m^3), h_s is the snow depth (m), T_s is the average temperature of the snowpack across all available snow layers (K), and T_m is the melting point of ice (273.15 K). The CC data set is retrieved from Rhoades (2023).

2.2. Selection of AR-Associated Runoff Events

To investigate the coastal runoff response to ARs, we selected eighteen 4-digit hydrological unit code (HUC) watershed basins along the U.S. West Coast (Figure 1a) (Jones et al., 2022). These selected watersheds are crucial as they represent diverse hydrological responses to AR events, allowing for a comprehensive assessment of how varying watershed characteristics influence runoff behavior. More information about selected HUC4 basins such as basin name and area size is provided in Supplemental Table S1 in Supporting Information S1. Within the selected watersheds, AR landfall activity is detected at each grid cell where the IVT exceeds 250 $kg\ m^{-1}\ s^{-1}$ (Rutz et al., 2014). Atmospheric river landfall events were flagged by marking AR time steps with a value of 1 and non-AR time steps with a value of 0. Events lasting less than one day (4 time steps) were neglected. Additionally, multiple events were merged into a single event if there was only one non-AR time step between them.

We acknowledge the detection uncertainty in ARs caused by different algorithm designs, which has been extensively discussed in previous studies (Lora et al., 2020; O'Brien et al., 2020; Rutz et al., 2019; Shields et al., 2018; Zhou et al., 2021). The AR detection method used in this study relies on an absolute IVT threshold

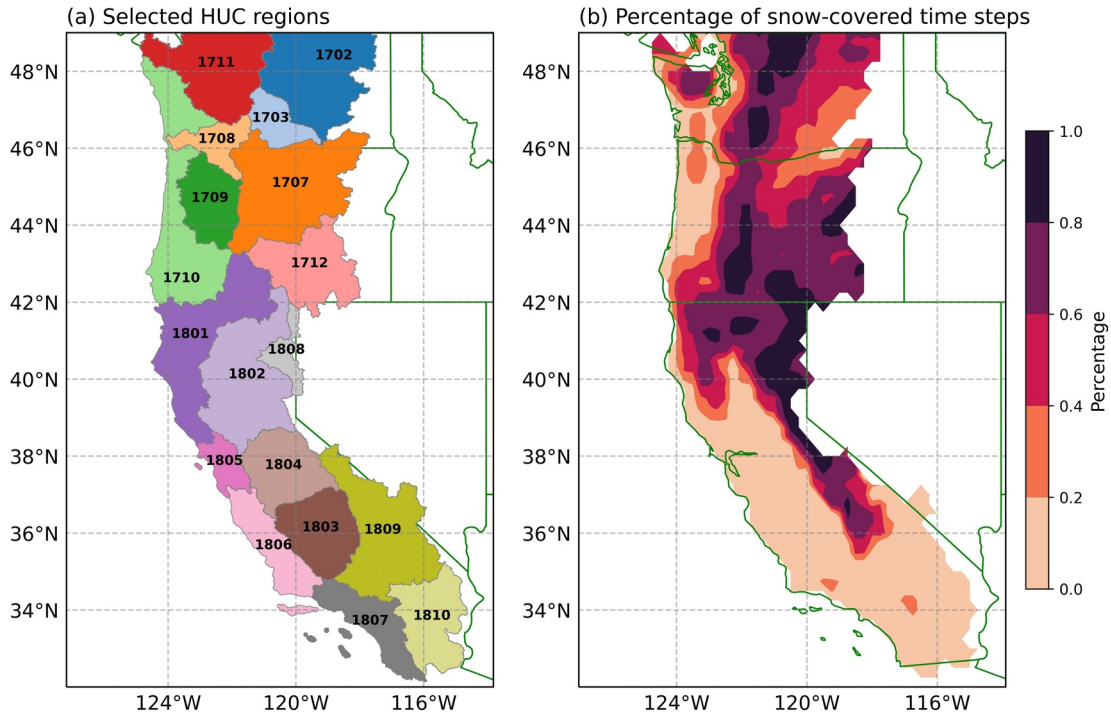

Figure 1. (a) Spatial map of the U.S. West Coast study region. The color and text denote the HUC4 watersheds. (b) Spatial map showing the percentage of time steps covered by snow with respect to total selected time steps in the 83 cool seasons analyzed.

and represents an Eulerian perspective of AR conditions. As explained in Ralph et al. (2019), the observer (or a grid cell) experiences the passage of an AR through the sequential change of meteorological and hydrological conditions. Consistent with Ralph et al. (2019), the term 'AR event' in this study refers to a period (i.e., the landfall period of the AR lifecycle) characterized by AR conditions over a given location. This Eulerian perspective on AR detection was selected for several reasons: (a) it is straightforward, intuitive, and practical for other forecast and prediction data sets; (b) it is relatively permissive, allowing for a large sample of possible AR-associated runoff time series especially for inland grid cells; and (c) it is consistent with (Ralph et al., 2019), making it effective for determining AR categories. A discussion on the sensitivity of the AR detection choice is included in Section 5.

Local runoff is greatly influenced by the seasonality of the snow fraction (Barnhart et al., 2016). Snowmelt contributes approximately 70% of total runoff in the mountainous regions of the U.S. West Coast (Li et al., 2017). To isolate the influence of snowmelt on runoff, contributions from snowmelt were excluded by considering only AR events that occur during the snow accumulation period of the cool season. The snow accumulation period is defined as the time before the SWE reaches its maximum, marking the end of the accumulation period and the beginning of the snowmelt period. Given that the onset of the snowmelt period has year-to-year variations (Cayan et al., 2001), there is a slight variation in the timing of the end of the snow accumulation period across each grid cell, primarily occurring between February and March.

Our discussion focuses on the relationship between ARs and the peak of associated runoff. The change in the runoff hydrograph caused by ARs is summarized in a schematic plot (Figure 2a). When an AR makes landfall, we record the runoff value, referred to as "runoff at AR landfall," along with the soil saturation degree and CC to represent land preconditions. During the AR landfall period, runoff increases over time, reaching a maximum value before gradually decreasing as the drainage flux flows downstream. To characterize ARs, we record grid-cell-based variables such as AR category, IVT, AR-induced precipitation, and AR duration (the period between AR landfall and termination on land). Additionally, we calculate the time gap between two AR landfalls as "interval days" to investigate the role of back-to-back ARs in modulating runoff response. In terms of runoff response, we focus on the peak runoff and incremental runoff defined as the difference between the runoff at AR landfall and the peak runoff. The period between AR landfall and peak runoff is termed "time to peak."

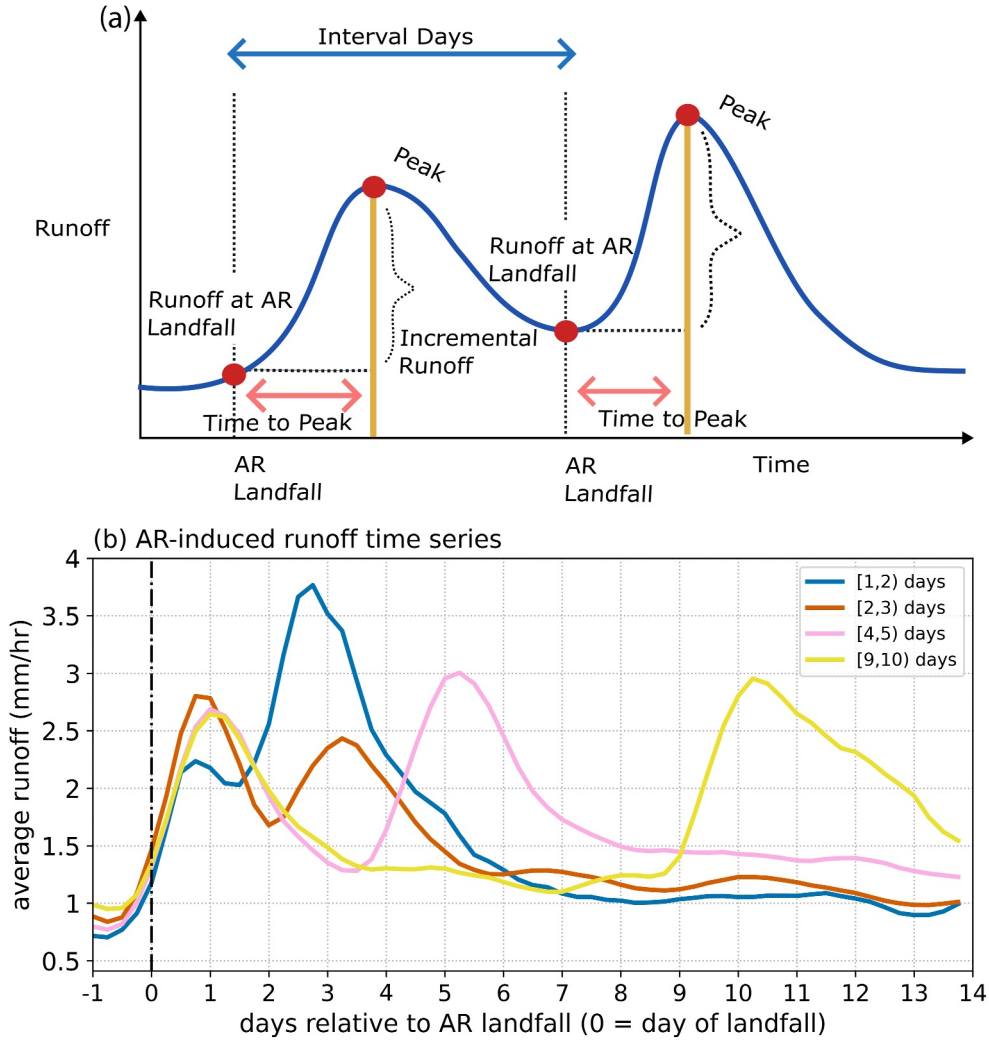

Figure 2. (a) Schematic plot showing the AR-induced runoff curve with metrics of interest marked. (b) Averaged AR-associated runoff time series grouped by selected interval days between atmospheric rivers (ARs) (time spacing between two landfalling AR events in the unit of days).

Approximately 75% of the time series reaches its maximum runoff before the termination of ARs, indicating that the time to peak is less than the AR duration.

During the snow-accumulating cool season, we select AR-associated runoff time series at grid cells within the U. S. West Coast HUC4 watersheds. The selection of AR-runoff events and associated metrics involves three steps.

1. AR Landfall Detection: For each grid cell within the region of interest, we detect AR landfall activity and generate AR landfall flags using a threshold of 250 kg m^{-1} s^{-1} on IVT. ARs lasting less than one day (4 time steps) are removed.
2. Runoff Time Series Selection: We identify the beginning of an AR landfall for each landfall period and select the runoff time series for 14 days (56 time steps) after the beginning of AR landfall. We choose 14 days as the cutoff point to sufficiently capture AR hydrological impacts upon careful investigation (See Section 3.1).
3. Variable Identification: For each runoff time series, we identify the AR-runoff metrics of interest. Time series where runoff remains constant or is monotonically increasing or decreasing imply that there is no AR influence on the runoff curve and therefore are neglected. The neglected time series is determined by the time peak runoff occurs after AR landfall. We identify time periods without AR influence as those in which peak runoff coincides with AR landfall (indicating that runoff remains constant or decreases monotonically) or occurs up to 2 days after the termination of AR conditions. About 32% of time series are removed from our further analyses.

Table 1
10-Fold Cross Validation Results for the Number of Basis Functions K_1 and K_2 for Each Runoff and Grid Cell Type Pairing

Grid cell type	Response	Accumulated precipitation (K_1)	Saturation degree (K_2)
No snow	Peak runoff	15	10
No snow	Incremental runoff	10	10
Snow	Peak runoff	6	9
Snow	Incremental runoff	6	6
HUC-averaged	Peak runoff	25	10
HUC-averaged	Incremental runoff	25	15

We selected approximately 287,000 time series over 83 cool seasons with about 37.5% of the time series indicating snow presence and 62.5% without snow. A grid cell is considered snow-covered if SWE is greater than zero. During the 83 cool seasons, most grid cells in the Pacific Northwest have been covered by snow for an average of 54% of the time steps with respect to the selected AR-related time steps over individual grid cells (Figure 1b). For grid cells in California, on average, about 25% of AR-related time steps have snow presence. Regarding spatial distribution, about 97% of grid cells in the Pacific Northwest have snow during over 90% of AR-related time steps. In addition to the grid cell time series, we also calculated domain-averaged time series for each HUC4 watershed to represent the domain response to ARs. It should be noted that spatial averaging will smooth out some strong signals. For example, extreme precipitation over grid cells may be smoothed and not accurately represented in the HUC-averaged perspective.

2.3. Runoff Regression Model

This study examines multiple factors that contribute to AR-induced runoff. We constructed a generalized additive model (GAM) (Hastie & Tibshirani, 1987) to predict changes in runoff under the combined effects of AR precipitation and land preconditions. We utilized the GAM because the relationship between land preconditions and AR precipitation on runoff is not necessarily linear (more discussion in Section 3). We constructed a separate GAM for each runoff variable (peak or incremental runoff) and grid cell type (grid cells without snow, grid cells with snow, or HUC-averaged) pairing. Here, we describe the process for one pair, specifically peak runoff from grid cells without snow, while the same process applies to the other pairs.

Let Y_i be the peak runoff from grid cells without snow for observation $i = 1, \ldots, N$. Because the peak runoff and incremental runoff data are skewed, we model the log response of both as a function of the accumulated precipitation, Precip_i, and saturation degree, Sr_i, using the GAM

$$\text{E}(Y_i) = \beta_0 + f_1(\text{Precip}_i) + f_2(\text{Sr}_i),$$

where $\text{E}(Y_i)$ is the expected value of peak runoff, β_0 is an intercept, $f_1(\text{Precip}_i) = \sum_{k=1}^{K_1} \beta_{1k} b_{1k}(\text{Precip}_i)$, $f_2(\text{Sr}_i) = \sum_{k=1}^{K_2} \beta_{2k} b_{2k}(\text{Sr}_i)$, $b_{1k}(\text{Precip}_i)$ and $b_{2k}(\text{Sr}_i)$ are thin plate splines for accumulated precipitation and saturation degree, respectively, that are specified prior to model estimation, β_1 and β_2 are regression coefficients, and K_1 and K_2 are the number of thin plate splines for accumulated precipitation and saturation degree, respectively. The GAM was estimated using the *mgcv* package (Wood, 2010) in *R* (R Core Team, 2023) using a double penalty to impose smoothing (Marra & Wood, 2011) and assuming normally distributed errors. To determine the number of basis functions K_1 and K_2 in each model fit, we performed 10-fold cross-validation based on minimizing the Akaike information criterion, deviance, and root mean square error and on model parsimony. The results of the 10-fold cross-validation are shown in Table 1.

3. Multifactor Impacts on Runoff Curve

In this section, we investigate various factors that influence the AR-associated runoff curves. The runoff response to ARs varies depending on AR characteristics and hydrological preconditions. Figure 3 shows the Pearson correlation coefficients of multiple variables against peak runoff.

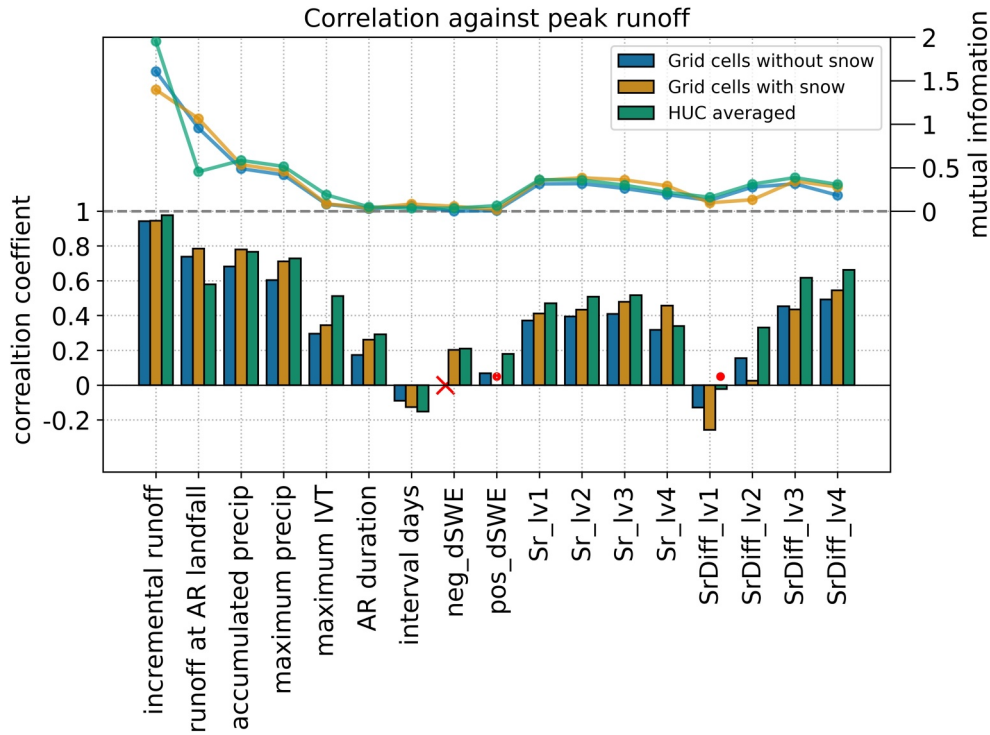

Figure 3. Pearson correlation coefficient (bars) and mutual information scores (lines) of selected variables against peak runoff for grid cells without snow, grid cells with snow, and hydrological unit code averaged time series. The acronyms "neg_dSWE" and "pos_dSWE" mean the negative and positive changes in snow water equivalent, respectively. The acronym "Sr_lv1" and "SrDiff_lv1" represent the saturation degree and change in saturation degree before and after atmospheric river (AR) landfall (using the peak saturation degree minus the one at AR landfall) at layer 1, respectively. The same applies to other Sr terms at layers 2–4. The red X marks the NaN value. All correlation coefficients have a p-value smaller than 0.01 except the ones marked by red dots.

Starting from the left of the *x*-axis of Figure 3, the results indicate that the peak runoff is closely correlated with both incremental runoff (1^{st} column) and runoff at AR landfall (2^{nd} column). The runoff value at AR landfall can be influenced by preceding ARs. For example, Figure 2b shows composites of selected runoff curves resulting from two consecutive ARs with different interval days. After the landfall of the first AR, the runoff increases to a peak value and then decreases. We observe different runoff magnitudes at the landfall of the second AR based on interval days with higher runoff values when interval days are small. For ARs that are 9–10 days apart, the runoff magnitude at the landfall of the second AR is close to the background value.

The 3^{rd}-7^{th} columns in Figure 3 are related to AR activity. The peak runoff is positively correlated with the accumulated precipitation during AR landfall. A high precipitation rate (labeled as 'maximum precip' in Figure 3) is also positively correlated with peak runoff, suggesting that higher precipitation intensity can lead to greater peak runoff. The accumulated AR-associated precipitation is influenced by the intensity ('maximum IVT') and landfall duration ('AR duration') of ARs. Results indicate that both intensity and duration are positively correlated with peak runoff, with comparable coefficients. Notably, a negative correlation is observed between interval days to prior AR events and peak runoff, suggesting that higher peak runoff occurs when multiple ARs happen within a short period (i.e., small interval days). However, the correlation with interval days is relatively lower compared to other AR-related variables. This is reasonable because the effect of interval days gradually dissipates as it increases (more in Section 3.1).

The 8^{rd}-17^{th} columns of Figure 3 represent the land preconditions including snow and soil moisture. The 8^{th} column indicates that snowmelt, reflected by the negative dSWE, can lead to higher peak runoff. A positive correlation is observed between peak runoff and positive dSWE, which means snowpack growth. We argue that this positive correlation may be due to the co-occurrence of snowpack growth and runoff increase during an AR landfall especially for grid cells without snow. The 10^{rd}-17^{th} columns show the correlation of all four

layers of soil saturation degree, which are consistently positive correlations with peak runoff, meaning that higher peak runoff occurs when the soil saturation degree is greater. This relationship arises because soil moisture storage is nearly full and more water becomes overland or subsurface flow, contributing to the peak runoff. Meanwhile, the change in saturation degree ("SrDiff_lv1 to 4"), calculated as the difference between the saturation degree (Sr) at peak runoff and AR landfall, shows an increasing trend in correlation coefficients with deeper layers mainly due to the increasing layer thickness and thus more soil water storage in deep layers, which controls the water table position and runoff generation from the saturation-excess flow. This difference in saturation degree between layers will be further discussed in Section 3.3.

We observe consistent results between the three grid cell types. The correlation coefficients of AR-related variables and land precondition variables are generally higher for HUC-averaged time series. This could be explained by the fact that the HUC-averaged time series are more likely to contain the upstream and downstream interactions of river networks. For example, the correlation with maximum IVT is lower in grid cells without snow, this could be due to (1) the maximum IVT over that grid cell is moderate or weak compared to the AR core or (2) the AR-related precipitation contributes to the infiltration of soil moisture. Similar correlation coefficients are found between incremental runoff and selected variables (Supplemental Figure S1 in Supporting Information S1). The only outstanding difference is that the incremental runoff shows a relatively lower correlation with runoff at AR landfall. This difference is expected, as runoff at AR landfall represents the system's hydrological memory from prior precipitation events and baseflow, whereas incremental runoff captures the immediate increment directly induced by the landfalling ARs.

In addition to the Pearson correlation analysis, we also assessed the relationships between the variables and peak runoff using mutual information. Mutual information is a measure that quantifies the amount of information gained about one random variable through another. Unlike Pearson correlation, which assesses only linear relationships, mutual information captures both linear and nonlinear associations between variables. The mutual information analysis corroborates many findings from the Pearson correlation results. Notably, the variables related to AR characteristics, including accumulated precipitation and maximum precipitation, exhibit high mutual information scores, further indicating their strong predictive value regarding peak runoff. Interestingly, the mutual information scores reveal that the interval days between AR events have a low predictive value regarding peak runoff as indicated by the near-zero mutual information. This suggests that although shorter intervals tend to correlate with higher peak runoff, the actual variability in peak runoff is not strongly determined by the interval days alone. Thus, although the timing of consecutive ARs may influence runoff responses, other factors likely play a more critical role in determining peak runoff levels. This underscores the complexity of the relationships among these variables. Additionally, the mutual information scores for the soil saturation degrees (columns 10^{th}-17^{th} in Figure 3) confirm the positive association with peak runoff. Higher saturation degrees in the soil lead to an increased likelihood of runoff generation, as demonstrated by the significant mutual information values for all four layers.

In conclusion, the mutual information analysis highlights the potential for identifying interactions between variables that may not be apparent through Pearson correlation alone. This reinforces the necessity for further investigation into nonlinear relationships (results in Section 2.3). In particular, the interactions between AR conditions, land preconditions, and their collective impact on runoff dynamics warrant deeper exploration.

3.1. Interval Days Between Consecutive Atmospheric Rivers

Studies show that ARs landfalling over the U.S. West Coast are temporally clustered at a greater-than-random rate (Slinskey et al., 2023). Densely packed AR clusters are more impactful because the time spacing between AR events, or interval days, is shorter, reducing the runoff response time to AR-associated precipitation. Zhou et al. (2024) indicate that dense AR clusters can result in increased runoff by up to 200% compared to sparse AR clusters. The spatial distribution of interval days between ARs is determined by the frequency of AR occurrences and the extent of AR inland penetration. During the Northern Hemisphere cool season, the most active AR season on the U.S. West Coast (Mundhenk et al., 2016), ARs generally make at least one landfall every 14 days (Figure 4). Interval days increase further inland as fewer ARs reach these grid cells. Overall, ARs reach the inland region approximately every 30 days during active seasons. The interval days between ARs increase from north to south in the focused region due to infrequent AR activity over southern California (Mundhenk et al., 2016).

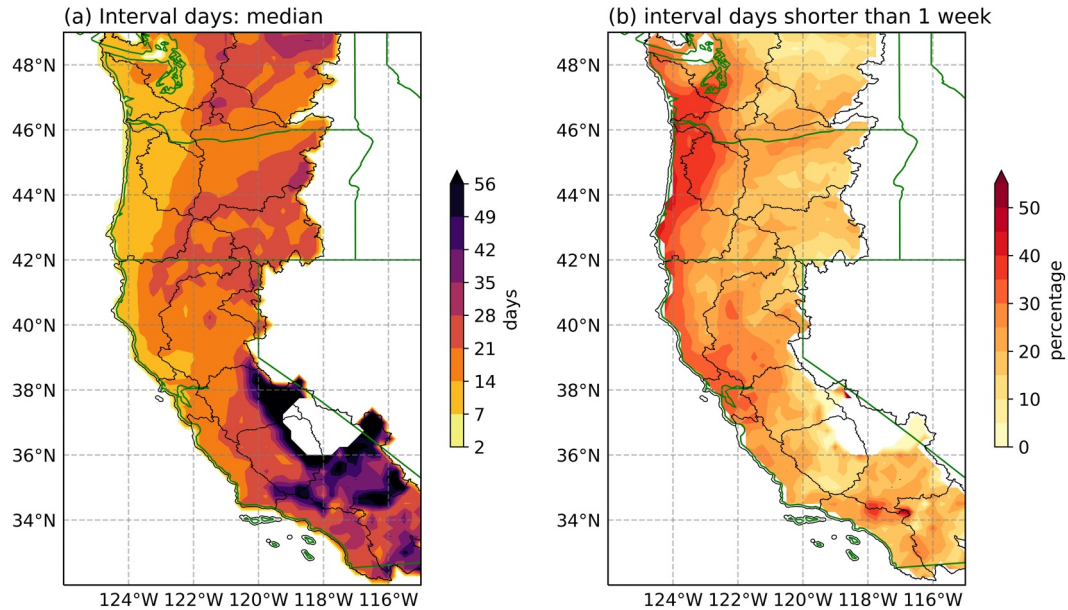

Figure 4. Spatial distribution of (a) the median of interval days since prior atmospheric rivers (ARs) and (b) percentage of ARs occurring within 1 week after the end of prior ARs. The percentage is compared to the total number of AR events.

We subset the AR-related runoff time series based on interval days (in increments of 2 days per bin) to the prior AR event (Figure 5). Figures 5a and 5b show the 95th percentile of runoff at landfall and peak runoff by different interval day groups. Here, we show the 95th percentile because groups with shorter interval days have longer tails toward higher values. More complete percentile distributions including the mean and the 25th, 99th percentile are provided in Supplemental Figure S2 in Supporting Information S1. Time series with interval days larger than 30 days are excluded from this discussion.

We observe strong peak runoff in shorter interval days especially for grid cells with snow (Figure 5a). For example, the 95th percentile of peak runoff by ARs occurring in 0–2 days after a prior AR is about 1.5 times stronger than those by ARs occurring 6–8 days after a prior AR. By examining the distribution of runoff at AR landfall and incremental runoff by AR, we see higher consistency in the distribution of runoff at AR landfall with peak runoff (Supplemental Figure S2 in Supporting Information S1). We hypothesize that runoff at AR landfall is modulated by the interval days to prior ARs as the soil moisture memory from the prior AR is still in place. Results indicate that grid cells covered with snow are much more sensitive to AR interval days. For snow-covered grid cells, the runoff magnitude at the landfall of the current AR decreases significantly as the interval day increases. Specifically, the 95th and 99th percentile of runoff at landfall when the current AR occurs within 2 days following the prior AR is nearly twice or even three times as much as within 6–8 days of prior ARs (Figure 5a and Supplemental Figure S2 in Supporting Information S1). This sensitivity in snow-covered grid cells is associated with snowmelt activity, which will be further examined later. Conversely, grid cells without snow show less sensitivity to interval days, indicated by the similar distribution among interval-day groups. The 99th percentile values suggest a relatively higher runoff at landfall from interval days shorter than a week (Supplemental Figure S2 in Supporting Information S1). We also present the HUC-averaged values to summarize the regional runoff response. Results indicate that the snow response is greatly smoothed in the HUC-averaged data (Figure 5a), although the 99th percentile magnitude decreases with increasing interval days. The peak runoff displays a similar distribution to runoff at landfall (Figure 5b) with grid cells covered by snow showing the highest sensitivity to interval days.

As the interval days increase, a consistent decreasing trend in surface soil saturation degree is observed in both snow-covered and no-snow grid cells (Figure 5c). We present the mean value of soil saturation in the interval day groups because the soil saturation has a fully saturated cap. Unlike runoff responses, the impact of interval days on surface soil saturation persists even when the interval exceeds 2 weeks. For regional averages, the saturation degree can vary by up to 15% when two ARs occur back-to-back within 2–4 days compared to when they occur

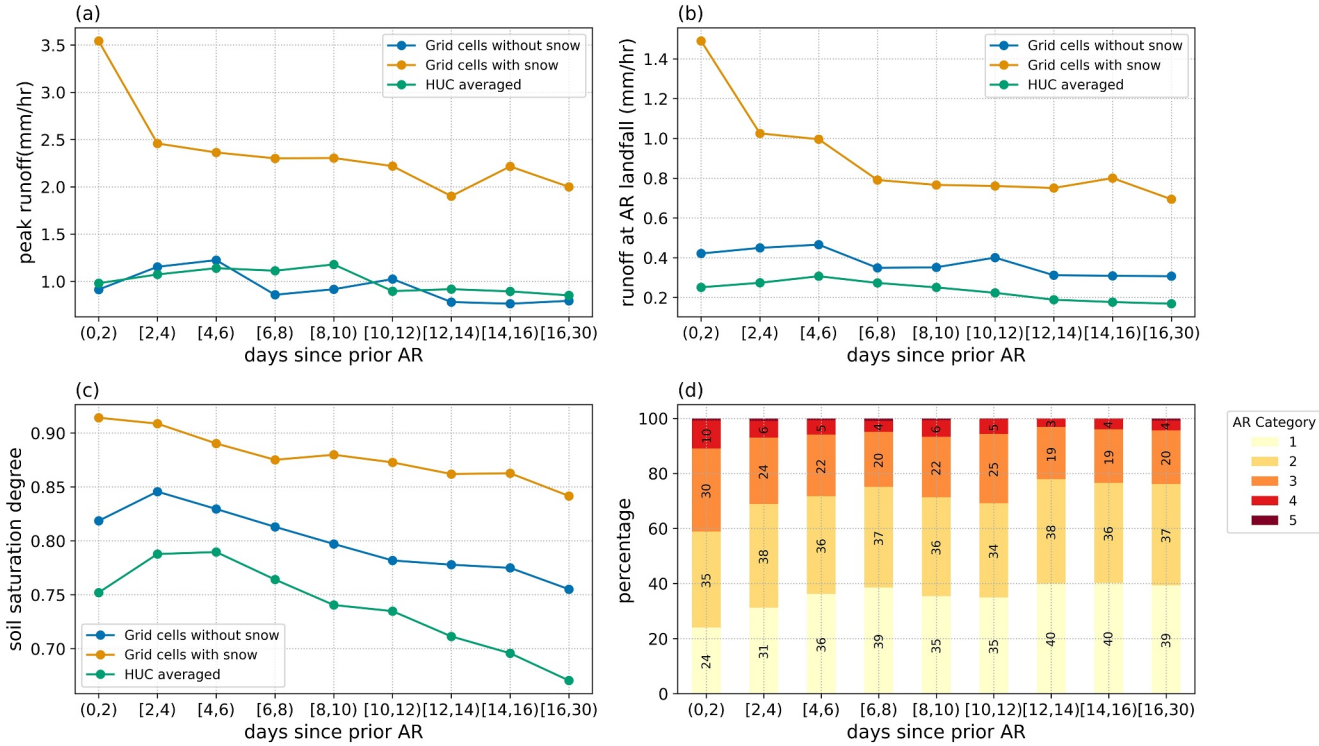

Figure 5. (a)–(c) Distribution of (a) runoff at atmospheric river (AR) landfall (mm/hr), (b) peak runoff (mm/hr), and (c) layer 1 soil saturation degree (%) based on interval days since prior AR events. Colored lines show (a)–(b) 95th percentiles and (c) mean of different subsets of data: grids without snow, grids covered by snow, and domain averaged by hydrological unit code regions. (d) Percentage distribution of AR categories (identified by grids) within each interval day group. The text indicates the percentage values contributed by each AR category.

2 weeks apart. Higher soil saturation with shorter interval days contributes to a higher peak runoff, as less precipitation is infiltrated into the soil and more is converted to runoff. A similar decreasing trend is observed in soil layer 2 but is not evident in the deeper soil layers (layers 3–4, Supplemental Figure S3 in Supporting Information S1), as subsurface flow has not drained soil water away from these depths.

In addition to the spacing to prior ARs, another factor contributing to the peak runoff is incremental runoff, which is attributed to the intensity of the current AR. Generally, the ratio of category 1–5 ARs is similar among interval-day groups larger than 6 days. For interval days shorter than 1 week, we observe a higher ratio of strong ARs (category >3) within shorter interval days (Figure 5d), indicating that the succeeding ARs that occur within short interval days are more likely to be of a higher category. However, the distribution of incremental runoff does not show a clear trend among interval-day groups except for a slight decrease in incremental runoff with increasing interval days of 0–7 days in snow-covered grid cells (Supplemental Figure S2 in Supporting Information S1).

Figure 5 emphasizes that ARs with shorter interval days to prior events are more likely to result in higher runoff and highly saturated soil, leading to an increased flood hazard. By grouping the time series into different interval days, we demonstrate that the influence of interval days diminishes as the interval increases. Groups with ARs occurring more than 7 days after a prior AR show a similar distribution of the runoff at landfall, suggesting that the memory of prior ARs is largely dissipated, minimizing the effect of interval days. Figure 4b shows the spatial distribution of interval days shorter than 1 week. Given the same AR category, areas with a higher frequency of short interval days potentially have higher runoff responses due to the memory of previous events. Areas with a high percentage (greater than 30%) include the west coast of the Pacific Northwest, the San Francisco Bay Area and two hotspots along the South Coast in the Transverse and Peninsular Ranges.

Further, we identify rain-on-snow (RoS) events in every grid cell to examine the role of snowmelt in modulating AR-induced runoff response. These determination metrics follow previous studies on RoS events (McCabe et al., 2007; Musselman et al., 2018). More specifically, a RoS event is defined when the grid cell has

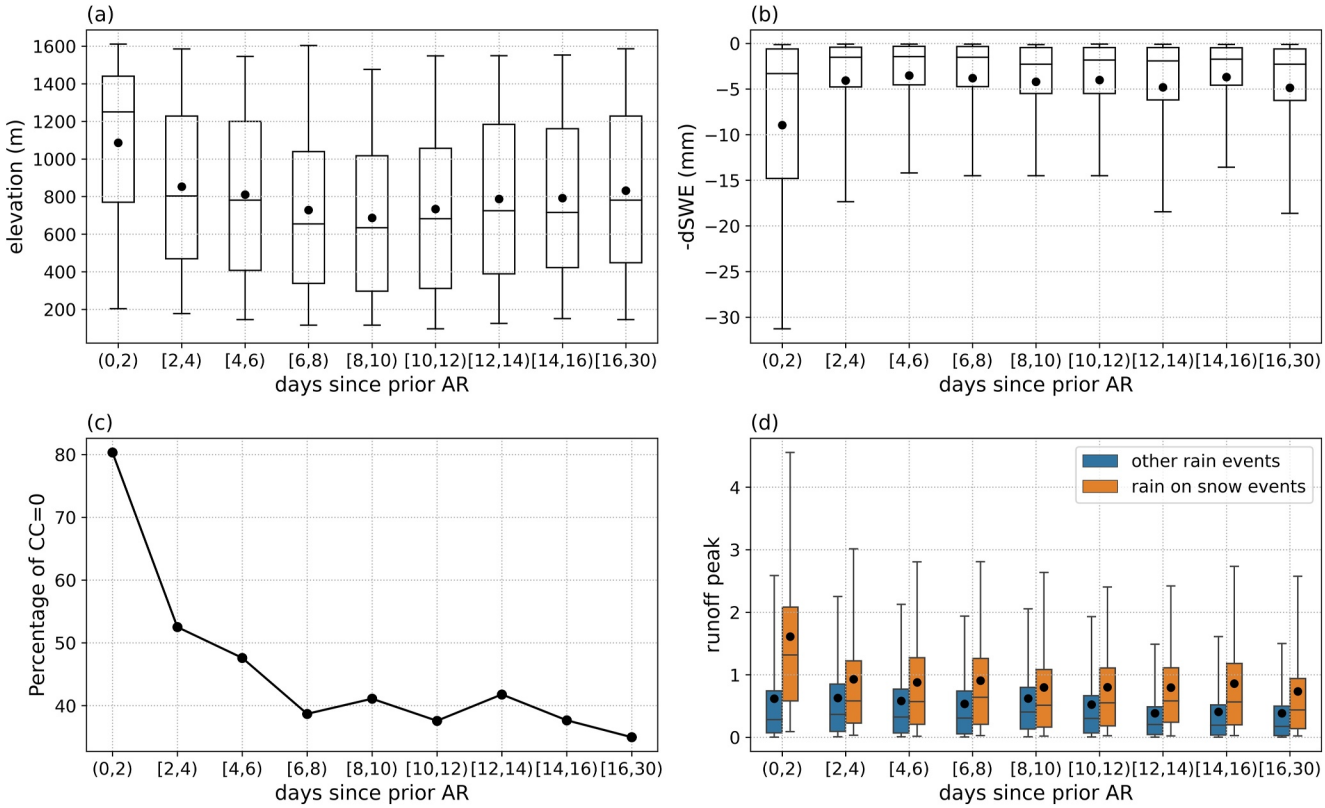

Figure 6. All panels show snow-covered grid cells only (a)–(b) Boxplots of snow-covered grids that have a negative change in snow water equivalent (SWE) during atmospheric river (AR) landfall for (a) elevation and (b) change value of SWE grouped by interval days since prior AR event. (c) Percentage of counts where cold content (CC) equals zero relative to all CC grid cells. (d) Boxplot of peak runoff (mm/hr) from (green bars) AR-associated rain-on-snow events and (orange bars) other AR-associated rainfall events. The whiskers of boxplots mark the 95th and 5th percentile of data. The 25th and 75th percentiles encapsulate the box region. The median and mean of data are denoted by the horizontal line and dot within the box region.

1. SWE greater than 10 mm,
2. Precipitation during AR landfall is greater than 0 mm, and
3. The sum of rainfall and snowmelt contributes to greater than 20% of the increase in runoff.

The snow ripeness (or how close it is to producing meltwater) can be measured by its CC. A CC value of zero indicates that the snow is ready to melt. Active snowpack usually exists in low-elevation regions with small magnitude CCs (Jennings et al., 2018). With back-to-back ARs, snowmelt occurs at much higher altitudes as interval days decrease (Figure 6a). All groups in Figure 6a are significantly different from their next group using *t*-tests with a p-value less than 0.01 except for groups with interval days between 10 and 12 days (p-value = 0.018). Groups in Figure 6b are also significantly different with a p-value less than 0.01 except for interval day groups 4–6 days (p-value = 0.047), 6–8 days (p-value = 0.015), and 8–10 days (p-value = 0.25). We find that shorter interval days between ARs can lead to a much higher proportion of ripened snowpack (Figure 6c). When two ARs occur within 2 days, about 80% of AR-affected snow-covered grid cells are ready to melt during the landfall of the succeeding AR (Figure 6c) likely due to increased temperatures from the preceding AR (Gonzales et al., 2022). Our results also indicate that the 2 m air temperature anomaly associated with ARs is higher with smaller interval days (Supplemental Figure S4 in Supporting Information S1). Additionally, the mostly saturated soil contributes to the runoff increase (Figure 5c). The percentage of ripened snowpack drops by 30% when interval days increase to 2–4 days. This is likely due to the snowpack having sufficient time to refreeze and build back CC. For interval days longer than a week (6–8 days in Figure 6c), the portion of ripened snowpack remains at a semi-constant level of 40%.

Generally, AR-associated RoS events lead to significantly stronger peak runoffs compared to other AR-associated rainfall events (Figure 6d). Specifically, the peak runoff from RoS events with interval days of 0–2 days is

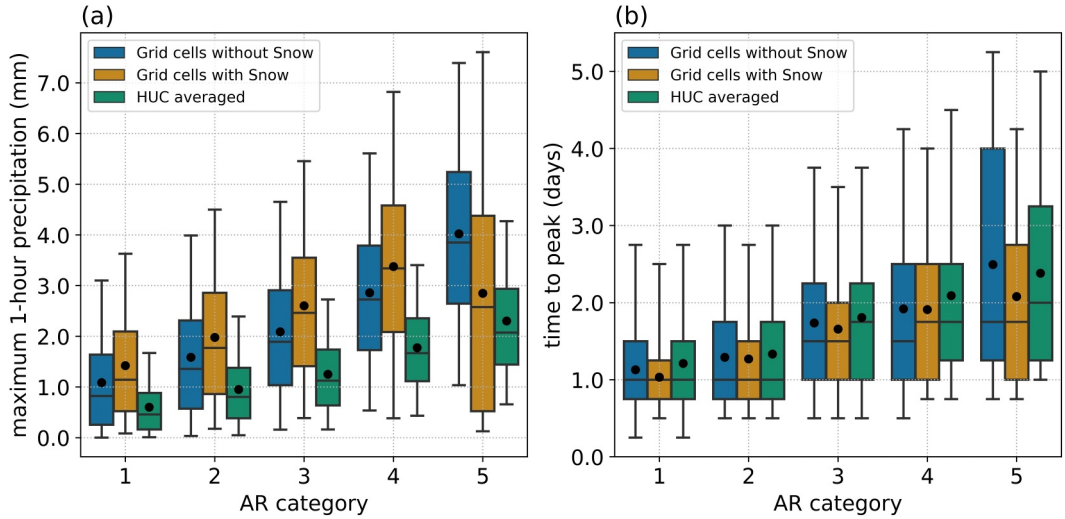

Figure 7. Boxplots of (a) maximum 1 hr precipitation (6-hourly averaged), (b) peak runoff (mm/hr), and (c) time to peak (days) grouped by atmospheric river (AR) categories. Time to peak is determined by the time between AR landfall and the peak runoff. Colors mark the three subsets of data: grid cells without snow, grid cells with snow, and grid cells averaged by Hydrological Unit Code regions. The whiskers of boxplots mark the 95^{th} and 5^{th} percentile of data. The 25^{th} and 75^{th} percentiles encapsulate the box region. The median and mean of data are denoted by the horizontal line and dot within the box region.

approximately twice as strong as non-RoS events. This high peak runoff is due to increased snowmelt represented by the negative change in SWE (-dSWE) (Figure 6b). For ARs with interval days of less than 2 days, the mean snowmelt amount is about twice that of other interval days. For interval days longer than 2 days, the distribution of snowmelt by AR is similar with a mean value of 5 mm. To summarize, the temporal clustering of ARs significantly impacts snow conditions for the succeeding ARs by increasing the proportion of ripened snowpack areas across elevations.

3.2. Atmospheric River Category

We apply the AR scaling metric developed by (Ralph et al., 2019) to determine AR categories, utilizing the maximum IVT and landfall duration of AR conditions in a given grid cell. During an AR landfall, the AR category is determined at each grid cell affected by the event, meaning that the same AR event can result in different categories across the impacted grid cells. The determination method is consistent with (Ralph et al., 2019) and effectively connects to the local extreme impact of ARs. To represent the regional response, we also determine the AR categories over the HUC regions using the maximum IVT and landfall duration for the entire region.

Besides the high correlation (Pearson correlation coefficient of 0.46 with a p-value of 0) found between ARs and their accumulated precipitation, we also observe increasing maximum one-hour precipitation with increasing AR category (Pearson correlation coefficient of 0.34 with a p-value of 0) in Figure 7a. The median values, indicated by the horizontal lines within each box, suggest that grid cells with snow tend to experience higher maximum precipitation rates compared to grid cells without snow across most AR categories. Additionally, the range of the whiskers, which indicates variability in precipitation rates, grows with higher AR categories, highlighting the influence of local hydrological conditions on precipitation extremes during AR events.

The time from AR landfall to reach peak runoff increases with AR categories (Figure 7b), because given similar IVT intensity, higher-category ARs have a longer duration over land (Ralph et al., 2019). On average, it takes about one day for runoff induced by category 1 ARs to peak, whereas it takes about 2 days for category 5 ARs. In some cases, it may take 4–5 days to peak. Grid cells with and without snow have a similar time for runoff to peak. Results indicate that higher AR categories cause a higher rate of increase in runoff, contributing to a greater flood risk due to shorter system response times (Miller, 1977).

Previous studies have discussed how the temperature of landfalling ARs affects changes in the snowpack of the U.S. West Coast. Guan et al. (2010) showed that ARs contribute about 30%–40% of SWE accumulation

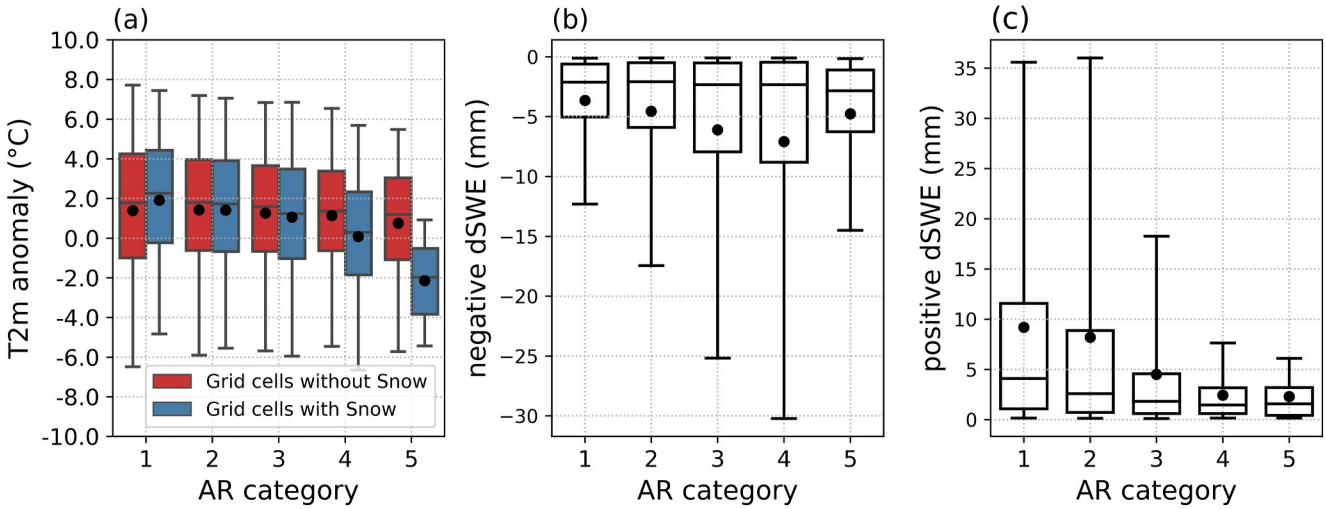

Figure 8. Boxplots showing the distribution grouped by atmospheric river category for (a) 2 m temperature anomaly (°C), (b) negative change, and (c) positive change of snow water equivalent (mm). (a) Include all grid cells and the colors denote snow presence in the grid cells. (b) and (c) only include grid cells with snow. The whiskers of boxplots mark the 95^{th} and 5^{th} percentile of data. The 25^{th} and 75^{th} percentiles encapsulate the box region. The median and mean of data are denoted by the horizontal line and dot within the box region.

annually with the contribution dominated by a handful of extreme events, which is supported by J. M. Hu and Nolin (2019). They also showed that the AR-related increases in SWE are negatively correlated with surface temperature. Gonzales et al. (2022) later discussed that the origin conditions of ARs (i.e., where their lifecycle starts over the ocean), rather than AR intensity, have a greater influence on the landfall temperature of ARs. Our results suggest a spread in positive and negative AR landfall temperatures (Figure 8a). The two-m temperature anomaly is calculated by removing the daily two-m temperature climatology of the grid cell. There are no significant discrepancies among grid cell types and AR categories except for category 5 ARs over snow-covered grid cells, where most of the temperature anomalies are below zero.

We further examine the distribution of snowmelt (represented by negative dSWE, Figure 8b) and snow accumulation (represented by positive dSWE, Figure 8c) by AR categories. The distributions of negative and positive dSWE exhibit different trends. For category 1–2, the magnitude of positive dSWE is about three times as strong as negative dSWE, suggesting that most categories 1–2 ARs contribute to building the snowpack. Category 3 ARs show comparable contributions to positive and negative dSWE with a slightly higher value in negative dSWE. In contrast, category 4–5 ARs largely contribute to negative dSWE, with values about 3–6 times stronger than positive dSWE. High flood hazards are posed when such strong AR events are accompanied by active snowpack and saturated soil (Henn et al., 2020; Rhoades et al., 2023).

To further understand AR category contributions to runoff, we subset the total runoff events into extremes and non-extremes. Extreme runoff cases are selected when the peak runoff exceeds the 95^{th} percentile of the HUC-averaged runoff value within the historical period (1940–2023). Extreme events have a higher percentage of higher AR categories compared to non-extreme events. The occurrence percentage of categories 3–5 ARs increases by about 100% for extreme events. We observe a 40% decrease in the occurrence percentage of category 1 ARs. Nevertheless, 25% of extreme runoff events are still associated with category 1 ARs (Figure 9a). Additionally, results show that ARs causing extreme runoff are approximately 30% more likely to be connected to RoS events compared to AR-related non-extremes. Especially, for weaker categories, 70% of extreme-runoff-associated category 1 ARs are RoS events (Figure 9b).

Figures 9c and 9d show the distribution of peak runoffs for extremes and non-extremes in different grid cell types. In both grid cell types, the peak runoffs of extremes are 3–5 times stronger than non-extremes. Notably, extreme peak runoff from category 5 ARs over snow-covered grid cells is eight times higher than non-extreme ones. We apply a linear regression to the mean value of peak runoffs as the AR category increases. Both extremes and non-extremes show positive slopes with increasing AR categories; however, the rate of increase in extreme runoff for grid cells with snow is 12.5 times stronger than that of those non-extreme runoff. For grid cells without snow, the rate of increase in extreme runoff is 3.5 times stronger.

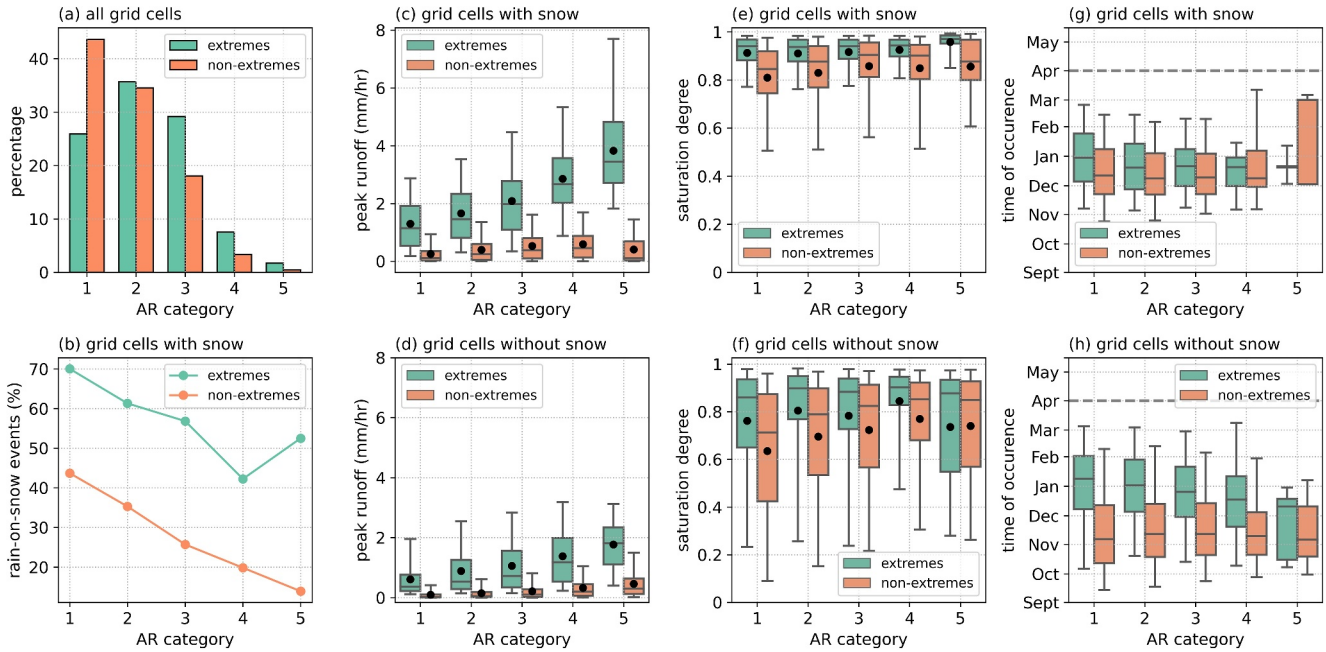

Figure 9. Comparison between AR-associated extreme runoff and total runoff by atmospheric river (AR) category. The first row is related to grid cells with snow and the second row is for grid cells without snow. (a) Percentage distribution of AR category including both grid cells with and without snow. (b) The relative percentage of the counts of rain-on-snow events to the total events under AR categories (c)–(h) Boxplots of (c)–(d) peak runoff (mm/hr) (e)–(f) soil saturation degree (%) at layer 1 (0–7 cm), and (g)–(h) time of occurrence for (green bars) extreme runoff events and (orange bars) non-extreme runoff events. The whiskers of boxplots mark the 95^{th} and 5^{th} percentile of data. The 25^{th} and 75^{th} percentiles encapsulate the box region. The median and mean of data are denoted by the horizontal line and dot within the box region.

Other factors affecting peak runoff intensity (extremes or non-extremes) include land preconditions and runoff seasonality. Figures 9e and 9f indicate that extreme runoff mostly occurs with high soil saturation degrees. Higher AR categories generally correspond to larger soil saturation degrees except for Category 5 ARs over snow-free grid cells as shown by the pattern of increasing mean soil saturation with increasing AR categories (Figures 9c and 9d). The saturation degree distributions by AR category are significantly different from each other with a p-value less than 0.01 except for category 1–2 ARs over grid cells with snow. The mean surface soil saturation degree associated with extreme runoffs is 10%–20% higher than that associated with non-extreme events except for category 5 ARs over grid cells without snow, where similar distributions of saturation degree appear in both extreme and non-extreme cases. This suggests that some extreme ARs can rapidly alleviate soil dryness, leading to extreme runoff even when the soil is initially dry.

We also analyze the timing of extremes and non-extremes to assess the influence of seasonality (Figures 9g and 9h). Note that we only include the snow accumulation period of the cool season in the discussion; thus, the runoff seasonality here solely refers to the cool season. For grid cells covered with snow, the mean occurrence time of extreme runoff is generally 2–3 weeks later than that of non-extreme runoff (Figure 9g). There is a shift toward an earlier time as the AR category increases for extreme runoff. For example, extreme runoff from category 1–2 ARs can occur from November to March, but extreme runoff from category 4–5 ARs mostly occur between November and mid-January. The timing discrepancy is more pronounced in grid cells without snow (Figure 9h). Most non-extreme runoff occurs in the early half of the cool season, between mid-October and mid-December, whereas extreme runoff happens in the latter half between December and late January or February. This may be attributed to the change in background runoff: as the cool season progresses, background runoff starts to build up (Bass et al., 2023), making it easier for weaker AR categories to generate extreme runoff.

3.3. Land Preconditions

Besides AR frequency and intensity, the land precondition before AR landfall plays a crucial role in the runoff response to ARs. By decomposing the peak runoff into runoff at AR landfall and incremental runoff, we find that both runoff fractions increase across the peak runoff percentiles (Figure 10a). The runoff at AR landfall can be

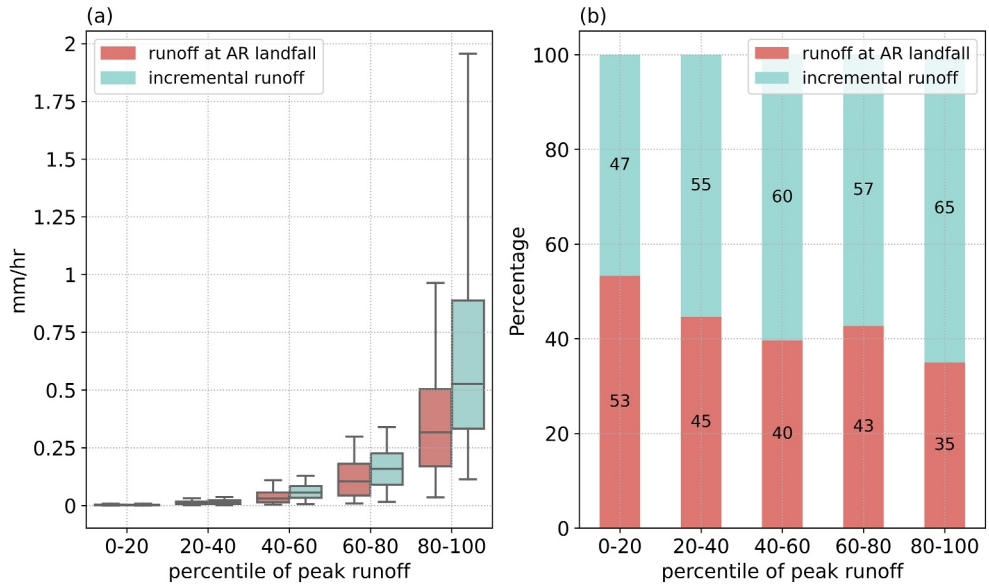

Figure 10. (a) Boxplots of runoff at atmospheric river (AR) landfall and incremental runoff grouped by percentile of peak runoff. (b) Percentage of contribution to peak runoff by runoff at AR landfall and incremental runoff. The whiskers of boxplots mark the 95^{th} and 5^{th} percentile of data. The 25^{th}, median, and 75^{th} percentiles encapsulate the box region with horizontal lines.

considered a combination of the memory from prior events and the background runoff, whereas the incremental runoff represents the increased runoff induced by the landfalling AR.

We show the distribution of all events because grid cells with and without snow have similar distributions (not shown). Comparable runoff magnitudes at AR landfall and incremental runoff are observed for 80% of the total events. Notably, for the top 20% of events, the incremental runoff is stronger than the runoff at AR landfall with the mean value of incremental runoff being twice as much as the latter. The contribution percentage of runoff at AR landfall decreases with higher peak runoff percentiles (Figure 10b). Overall, the runoff at AR landfall contributes about 35%–50% of the peak runoff. Figure 10 indicates that strong peak runoff events (e.g., above the 80^{th} percentile) require both high runoff pre-landfall and a significant runoff increment from strong AR events.

Figure 9 indicates that extreme peak runoffs occur with high surface soil saturation degrees. Here, we show the distribution of soil saturation degrees across all ERA5 soil layers (Figure 11). A positive connection is observed between soil saturation degree and peak runoff: higher peak runoff is accompanied by more saturated soil. For small peak runoffs (below the 20^{th} percentile), the soil is less saturated across depth levels with the median saturation degree around 50%–60% between 0 and 100 cm.

For intensive peak runoffs, the soil is much more saturated, with the saturation degree across layers reaching about 90%. This high saturation greatly reduces soil infiltration and increases the likelihood that precipitation contributes more directly to runoff. The discrepancies in soil saturation among peak runoff percentiles are relatively smaller in soil layer 4, likely because it is a much deeper subsurface layer and contributes less to peak runoff, which is usually dominated by faster overland flow and subsurface interflow (Tao & Barros, 2013).

The top 7 cm of soil shows the most immediate response when an AR makes landfall. This layer experiences the greatest change during an AR event with the saturation degree increasing by about 20% (Figure 11b). The changes in layers 1-3 decrease as the starting saturation degree approaches full saturation. The occurrence of the greatest change in saturation degree varies across the layers. Soil layer 1 shows the greatest increase when the peak runoff is moderately weak (20^{th}-40^{th} percentile). The biggest increase in soil layer 2 appears with moderately stronger peak runoff (60^{th}-80^{th} percentile). Finally, the greatest increase in soil layers 3–4 occurs with peak runoff over the 80^{th}-100^{th} percentile. This variation implies that the infiltration depth is jointly determined by precipitation and antecedent soil moisture, thereby influencing the runoff response (Guo, 2020).

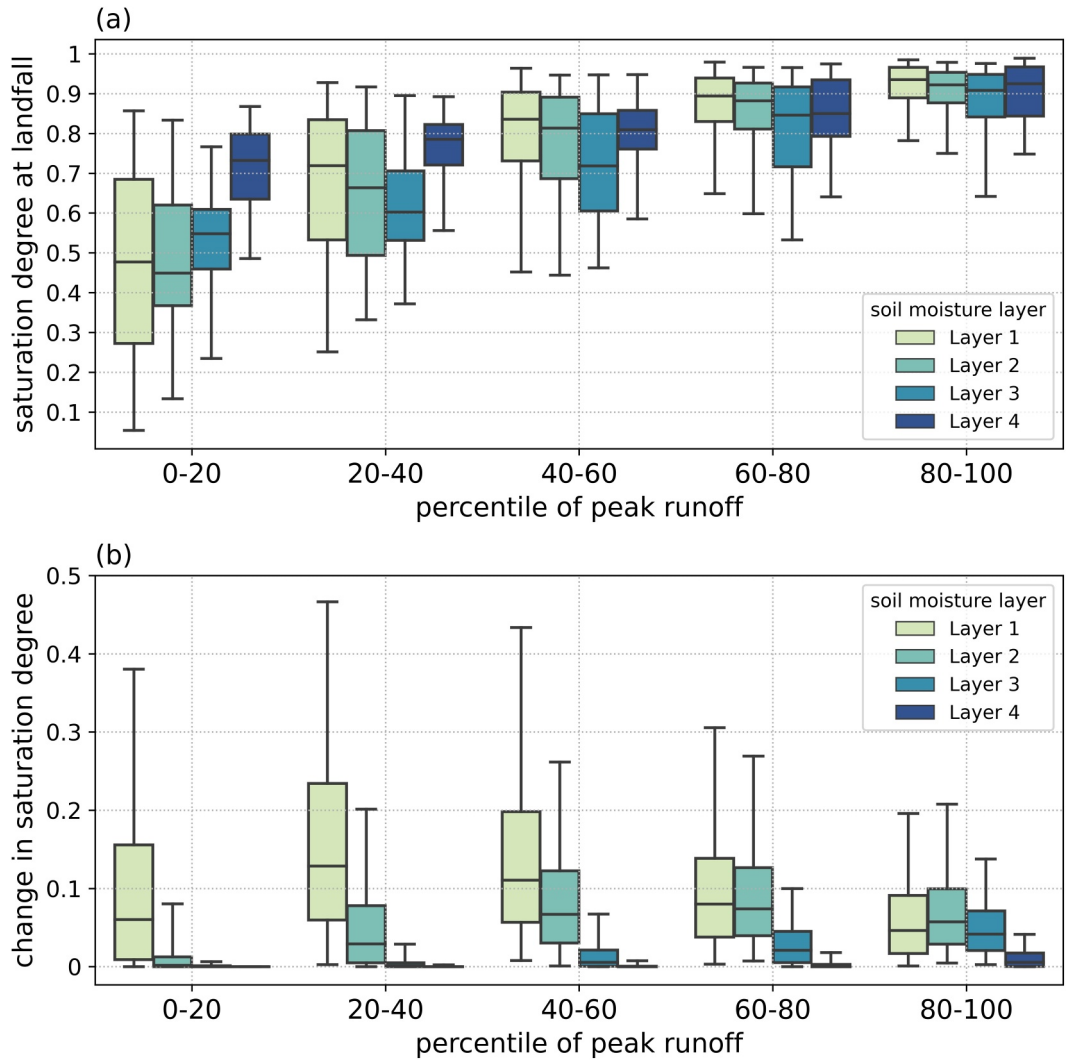

Figure 11. Boxplots of (a) soil saturation degree (%) at atmospheric river (AR) landfall and (b) changes in saturation degree between AR landfall and peak runoff. Colors mark the soil layers. The whiskers of boxplots mark the 95^{th} and 5^{th} percentile of data. The 25^{th}, median, and 75^{th} percentiles encapsulate the box region with horizontal lines.

For grid cells covered with snow, the intensity of peak runoff is closely connected to the ripening level of snow. Figure 12a shows the percentage of active snowpack by peak runoff percentiles. Weaker peak runoffs (below the 60^{th} percentile) have much less active snowpack with less than 30% being active. For stronger peak runoffs (above the 80^{th} percentile), about 40% of snow-covered grid cells have active snowpack. Consequently, more than 50% of strong peak runoff events are associated with RoS (Rain-on-Snow) events (Figure 12b). The connection between peak runoff intensity and snowpack is consistent with previously discussed results: high peak runoff is more likely to occur under conditions of saturated soil and a ripened snowpack, which could result from back-to-back ARs (Figures 5 and 6).

4. Statistical Quantification of Runoff Response

Section 3 discusses how AR-induced runoff changes by the saturation degree and AR characteristics. We show that high soil saturation and high AR category can lead to a higher increase in runoff. However, the combined effect of soil saturation and AR precipitation on runoff is still not clear. Notably, weak AR categories can also produce extreme runoff when nearly saturated soil is present due to preceding ARs. Here, we construct a GAM particularly to quantify the impact of soil saturation (represented by saturation degree) and AR precipitation (represented by accumulated precipitation during landfall) on peak runoff and incremental runoff. The reason for

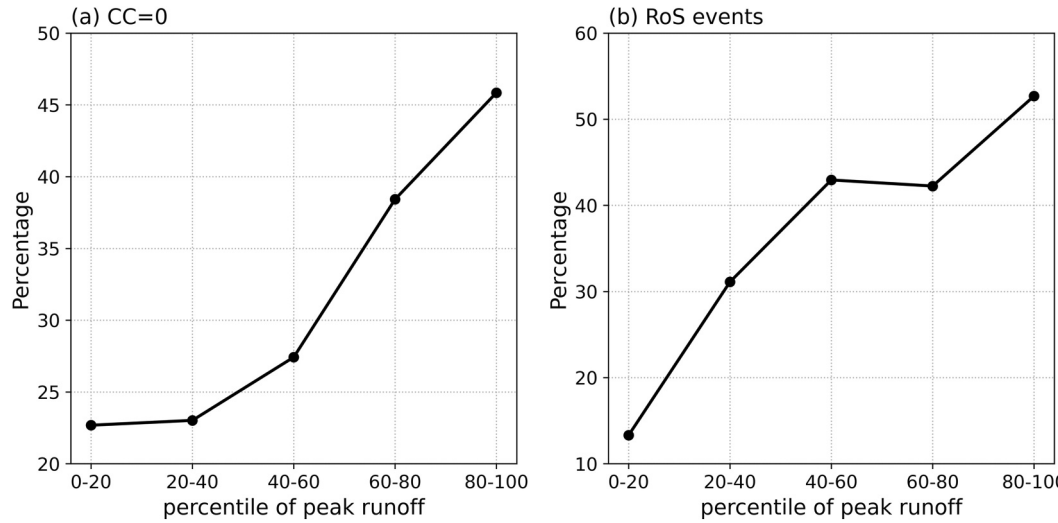

Figure 12. Percentage of (a) counts of grid cells with cold content equals zero at atmospheric river landfall and (b) counts of rain-on-snow events, grouped by percentiles of peak runoff. The calculation only considers grid cells covered with snow.

selecting these two variables is that they show relatively high mutual information with runoff (Figure 3 and Supplemental Figure S1 in Supporting Information S1).

To visualize the relationship between saturation degree and accumulated precipitation for each runoff variable and grid cell pair, we compute the estimated mean response and 95% confidence interval as a function of accumulated precipitation, ranging from 0 to 200 mm, for a given percentile of saturation degree, the 25^{th}, 50^{th}, 75^{th}, 95^{th}, and 99^{th}.

Figure 13 shows a consistent increase in both peak and incremental runoff as accumulated precipitation increases. Additionally, for multiple runoff variables and grid cell type groupings, the runoff response significantly differs depending on the saturation degree percentiles, as indicated by the 95% confidence intervals not overlapping, which means that the preconditioning of the soil significantly impacts the runoff response. For grid cells without snow (Figures 13a and 13d), the peak runoff is stratified for all percentiles except the 95^{th} and 99^{th}, which overlap for nearly all values of accumulated precipitation. However, for incremental runoff, the delineation between percentiles is less clear, with only the 25^{th} percentile being clearly different for all values of accumulated precipitation. For grid cells with snow (Figures 13b and 13e), the stratification based on percentiles for both peak and incremental runoff is the same as for the corresponding response when considering grid cells without snow. One difference is the shape of the response curves, where the curves for grid cells without snow do not appear to flatten as accumulated precipitation nears 200 mm.

For HUC-averaged data (Figures 13c and 13f), both runoff variables are stratified based on the increasing percentile, with the 25^{th} percentile resulting in the lowest mean runoff and the 99^{th} in the highest. Interestingly, the significance of the difference between saturation degree percentiles for both peak and incremental runoff for HUC-averaged cells depends on the accumulated precipitation. For runoff variables, the confidence intervals widen as accumulated precipitation increases, and there is no clear significant difference between the saturation degree percentiles when accumulated precipitation is greater than 175 and 125 mm for peak and incremental runoff, respectively. Additionally, for HUC-averaged data, the response curves appear to flatten or decline as accumulated precipitation approaches 200 mm, which we attribute to the lack of observations with accumulated precipitation values greater than 200 mm (see Supplemental Figure S5 in Supporting Information S1), and the uncertainty in the mean response widens, which is also a product of fewer observations for high values of accumulated precipitation. One possible explanation is that the spatial averaging smooths out the extreme signals so that the sample size for such strong accumulation precipitation is smaller (Supplemental Figure S5 in Supporting Information S1).

In summary, by analyzing the estimated mean responses and 95% confidence intervals for peak and incremental runoff across varying saturation percentiles and accumulated precipitation levels, we observe a consistent

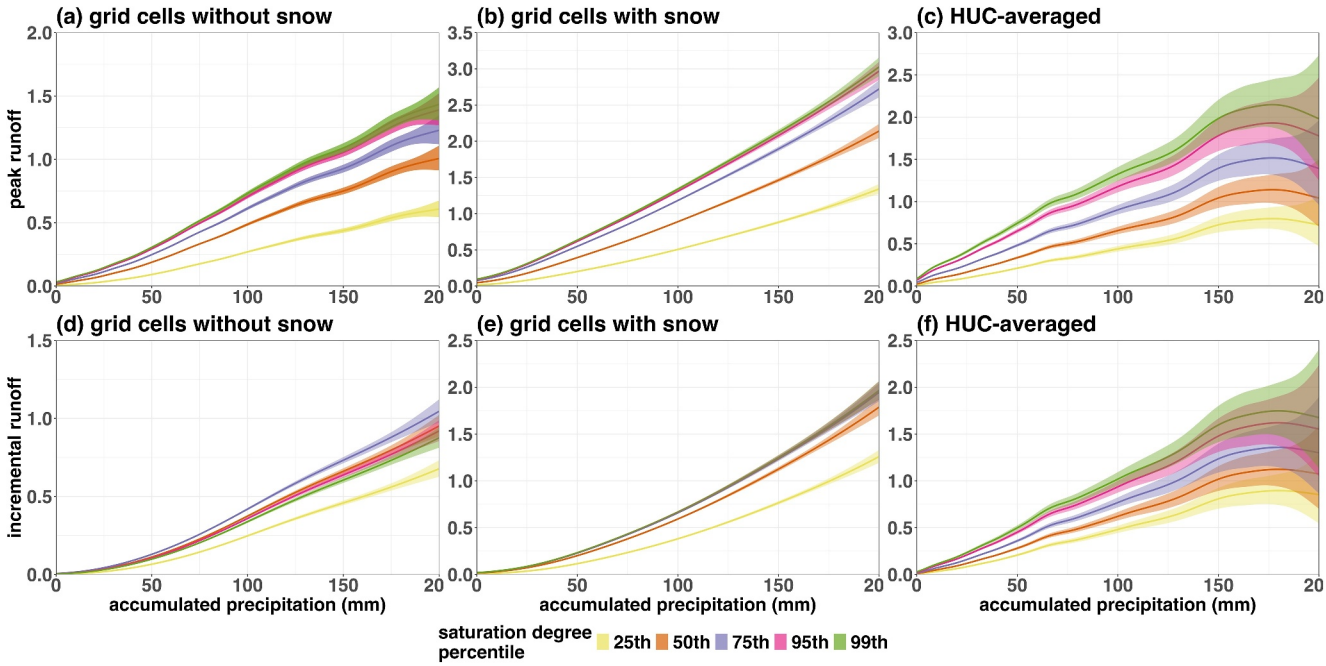

Figure 13. Mean response (solid line) and 95% confidence intervals (shaded area) for peak runoff (a–c) and incremental runoff (d–f) for increasing values of accumulated precipitation and different levels of soil saturation degree (color of lines and shaded region) for grid cells without snow (left column), grid cells with snow (middle column), and grid-cell averages by Hydrological Unit Code regions (right column).

increase in runoff as AR precipitation rises. Notably, the distinct stratification of runoff responses based on saturation degree indicates that soil preconditioning plays a critical role in determining runoff outcomes. As accumulated precipitation approaches higher thresholds, the confidence intervals widen, and distinct differences among saturation percentiles become less evident, suggesting that extreme conditions may dilute the effects of saturation. This analysis underscores the importance of soil saturation in modulating runoff responses during AR events while also acknowledging the limitations associated with high precipitation observations.

5. Sensitivity Discussion

The large uncertainty in AR characteristics could originate from AR detection uncertainty, which can, in turn, affect the interpretation of AR-runoff relationships (O'Brien et al., 2020; Rutz et al., 2019; Shields et al., 2018; Zhou et al., 2021). Different AR detection algorithms (ARDTs) are developed based on specific questions of interest. For example, restrictive algorithms highlight the core area of ARs with the strongest intensity, which can be used to understand the lifecycle activity and the physical development of ARs. Meanwhile, permissive algorithms tend to include more grid cells impacted by AR conditions, which are useful from the impact perspective of ARs (e.g., precipitation that occurs away from the AR core region). Previous studies (e.g., Figure 6 in Rutz et al. (2019)) emphasized that only a handful of the permissive ARDTs can identify AR conditions over the interior region of the coastal western U.S., which is the area located about 10° away from the coastline and embedded within complex topography (e.g., California Sierra Nevada). This limitation, however, restricts our selection of ARDTs because it is essential to include AR hydroclimate responses in these interior grid cells. To address the detection uncertainty in this study, we include two ARDTs that are developed by Guan and Waliser (2015) (denoted as tARget) and Ullrich et al. (2021) (denoted as Tempest) to compare with our selected method of absolute threshold on IVT (denoted as IVT250). The tARget algorithm uses multiple criteria, including an 85^{th} percentile relative threshold on the IVT field, constraints on IVT direction, and the geometric shape. It is one of the most permissive algorithms among all ARDTs (Zhou et al., 2021). The Tempest algorithm applies an absolute threshold on the Laplacian of IVT and a threshold on the geometric shape. The frequency of ARs detected by Tempest along the U.S. West Coast falls within the median range among all ARDTs (Rutz et al., 2019). The period for the sensitivity test is the cool seasons from 1985 to 2014.

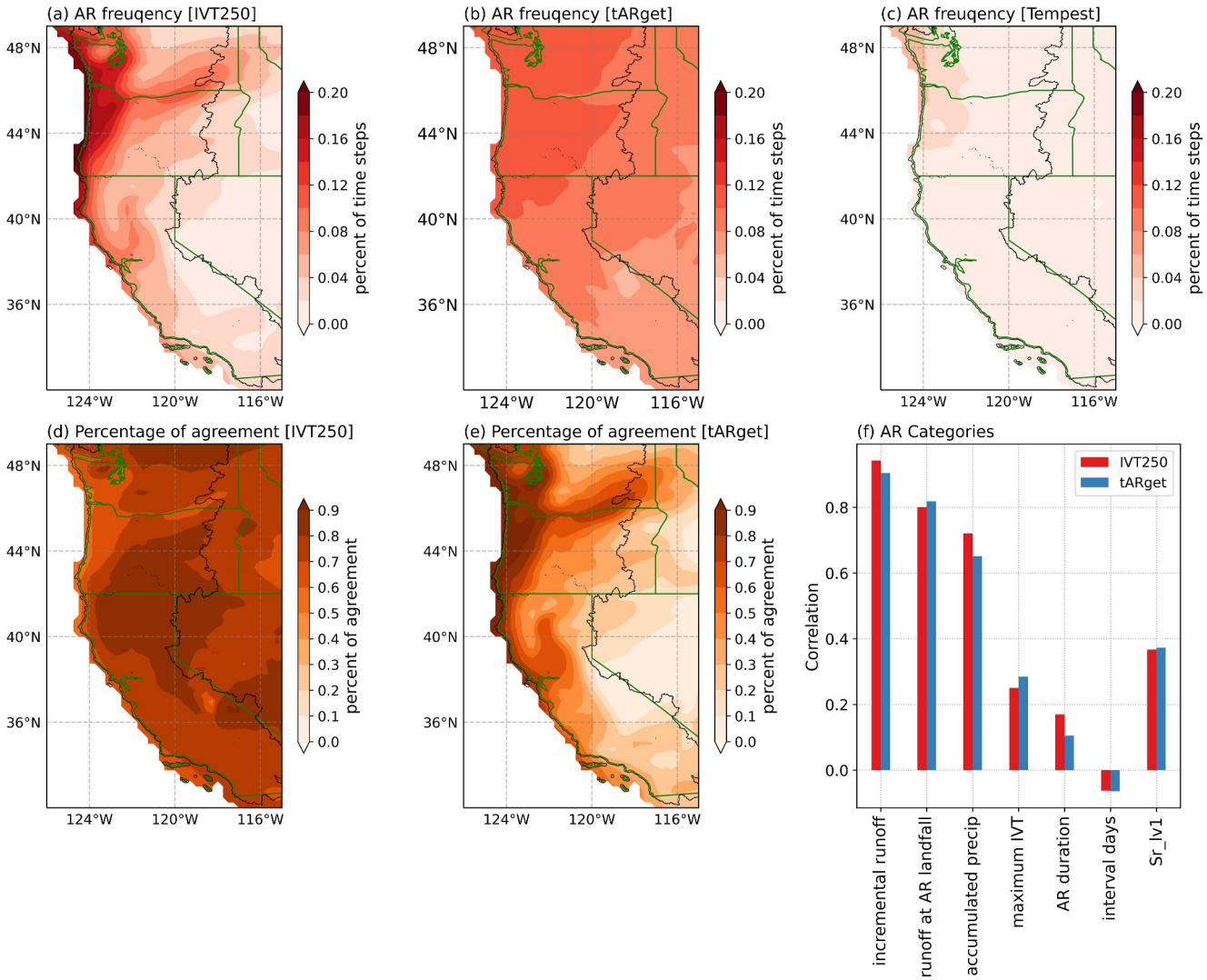

Figure 14. (a)–(c) Atmospheric river (AR) frequency (percent of time steps) of the focused season for (a) absolute integrated vapor transport threshold (IVT250), (b) tARget, and (c) TempestExtreme (TE) (d)–(e) Percentage of agreement for (d) IVT250 against tARget, and (e) tARget against IVT250. (f) Density distribution of AR categories among the three AR detection algorithms.

All three ARDTs show higher AR frequency over the Pacific Northwest, but the amplitude of AR frequency differs (Figure 14). Atmospheric river frequency using IVT250 shows the highest amplitude with AR conditions occurring on average 16% of time steps over the Pacific Northwest and 2%–8% over California (Figure 14a). The AR frequency by tARget is in weaker amplitude over the Pacific Northwest with AR conditions happening in about 10% of time steps, but it has a higher amplitude over California, with about 6%–10% of AR-affected time steps (Figure 14b). The Tempest ARs show the smallest amplitude over the U.S. West Coast compared to the other two ARDTs with most grid cells having less than 4% of AR-affected time steps. The comparison suggests that Tempest may not be the most suitable ARDT for this study, likely because its use of an IVT Laplacian threshold combined with geometric shape limits its ability to detect AR conditions over land.

Next, we calculate the percentage of agreement between IVT250 and tARget. We define the agreement between the two ARDTs as occurring when both detect an AR condition at the same time step over the same grid cells. Figures (Figures 14d and 14e) show the percentage of time steps in agreement between the two ARDTs. The results suggest a high percentage of agreement between IVT250 and tARget. Specifically, for IVT250, most grid cells over the U.S. West Coast have more than 70% of time steps consistent with ARs detected by tARget. For the tARget algorithm, the higher agreement appears near the coastline, with more than 50% of time steps agreeing

with IVT250. However, the percentage of agreement drops as one moves further inland. Additionally, we find a high consensus in the density distribution of AR categories between IVT250 and tARget (not shown).

Despite the high agreement in spatial distribution between IVT250 and tARget, we observe a disagreement in the number of selected time series. Over 1985 to 2014, IVT250 returns about 123,000 time series, whereas tARget has 240,000, which is almost twice as many as IVT250. However, the correlation coefficients of peak runoff against AR-related variables and land preconditions show high agreement between IVT250 and tARget (Figure 14f), indicating the robustness of the results presented in this study.

To summarize, we observe high agreement in the detection of AR conditions between IVT250 and tARget, which is one of the most widely used permissive ARDT. Although tARget has a larger sample size in AR-related hydrologic time series, we use IVT250 because of its ease of application and provides instantaneous AR detection on data sets such as reanalyses and model forecast outputs.

6. Summary and Discussion

In this study, we extensively investigate the contributing factors to runoff response from ARs over the U.S. West Coast. Results demonstrate that high-category ARs can result in a stronger increase in local runoff consistent with previous studies (Chen & Leung, 2020). By examining the distribution of related variables by AR categories, we show that higher AR categories have higher maximum one-hour precipitation rates and result in greater incremental and peak runoff. Besides the direct impact of the AR category, we emphasize that the occurrence frequency of ARs, land preconditions (including soil moisture and the ripeness of the snowpack), also play crucial roles in modulating the runoff response.

Runoff responses from weaker AR categories are more sensitive to land preconditions because the conditions before AR landfall establish the baseline runoff state, which may be compensated for if the AR is strong enough. We demonstrate that the upper percentiles of peak runoff occur when the soil is already in a nearly saturated state. Higher peak runoffs also lead to deeper soil infiltration.

We observe different runoff magnitudes between grid cell types (with snow or without snow) in response to ARs. The increased runoff is of much higher magnitude in grid cells with snow due to the contribution from snowmelt. For grid cells covered with snow, high-runoff-peak events are mostly associated with RoS events especially for weaker ARs. Although high-category ARs are more likely to induce extreme runoff, we find that weaker AR categories (such as categories 1 and 2) can also lead to extreme runoff given pre-existing high runoff conditions or significant snowmelt amounts. Snowmelt from ripened snowpacks contributes to incremental runoff, greatly increasing the potential for extreme runoff. We also highlight that there is a much higher ratio of active snowpack when two ARs occur within a week. Some ARs contribute to snow accumulation as the moisture they carry cools when passing over mountains. Our results show that ARs contributing to the growth of the snowpack are mostly category 1–2 ARs.

We apply a regression model to examine the combined effect of AR precipitation and land preconditions on runoff responses. Uniformly increasing trends in peak runoff and incremental runoff are observed across grid cell types as AR precipitation increases. Clear distinctions are noted with different soil saturation levels, emphasizing the importance of soil dryness when assessing the impacts of AR landfall. When evaluating landfall impacts using the AR category scale (Ralph et al., 2019), it is crucial to include land preconditions (soil dryness and snowpack ripeness) for a more accurate estimation of local runoff response and flood hazard.

Our results have significant implications for the risk assessment of ARs by examining relevant factors that contribute to runoff response. These factors, including AR characteristics (intensity, occurrence frequency, and precipitation) and land preconditions (soil saturation and snowpack), could be incorporated into prediction models to assess AR-induced runoff curves. Additionally, the current study provides model evaluation metrics for runoff response to ARs. Beyond comparing individual variables, the GAM regression model is a valuable tool for evaluating the effects of multiple variables (AR characteristics plus land conditions) on runoff.

Several limitations are noted in this study. First, some runoff time series were not included due to the lack of indication of AR-induced changes, which may lead to an incomplete representation of AR impacts. Why some AR-influenced grid cells showed no evident runoff change is not discussed in this study. Second, the permissive AR detection algorithm used in this study may include some rainfall events that are not classified as ARs by other

detection algorithms, potentially overestimating AR-related runoff. Third, the ERA5 land surface model estimates runoff using a single-column model without subsurface transfer of water between grid cells, which may not fully capture the complexity of real-world hydrological processes nor the influence of water management and infrastructure on runoff.

The discussion on the interval days between consecutive ARs reflects the specific land conditions set by prior ARs. The impact of interval days between ARs is prominent until two ARs are a week apart or more. When two ARs occur back-to-back within a week, the runoff response to the succeeding AR is greatly intensified due to the "memory" of the preceding AR, characterized by higher runoff values and increased soil saturation. We observe a slightly higher ratio of moderate and strong ARs occurring in back-to-back sequences, which could exacerbate their already hazardous land impacts. It has been shown that back-to-back AR clusters may occur more frequently in warmer climates (Bowers et al., 2023). Key questions to be addressed include how the mean-state land conditions prior to AR landfall will change with warming temperatures and whether AR-associated runoff will become more sensitive to back-to-back ARs in the future.

Challenges remain in quantifying and understanding the impacts of preceding ARs, as 30%–50% of ARs along the West Coast occur in succession (i.e., two ARs within a week; Figure 4). To address this challenge and isolate runoff responses from the preceding and succeeding ARs, our ongoing research focuses on building a machine learning model to predict the AR-induced runoff curve using inputs from AR characteristics and land preconditions. Additionally, this model has the potential to be applied to Earth system models as a diagnostic tool for land-atmosphere interactions and to assess the influences of climate change on these interactions.

Data Availability Statement

The ERA5 hourly data can be retrieved from https://cds.climate.copernicus.eu/datasets/reanalysis-era5-pressure-levels?tab=overview. The ERA5 cold content is calculated and archived in https://portal.nersc.gov/archive/home/a/arhoades/Shared/www/ERA5_Cold_Content.

Acknowledgments
Lawrence Berkeley National Laboratory is managed by the University of California for the U.S. Department of Energy under contract DE-AC02-05CH11231. This study was funded by the Director, Office of Science, Office of Biological and Environmental Research of the U.S. Department of Energy Regional and Global Climate Modeling Program (RGMA) and MultiSector Dynamics Program Areas. YZ, JSN, AMR, MDR, and WDC are supported by "Calibrated and Systematic Characterization, Attribution and Detection of Extremes (Calibrated and Systematic Characterization, Attribution and Detection of Extremes)" Science Focus Area. AMR was also funded by the "An Integrated Evaluation of the Simulated Hydroclimate System of the Continental US" (HyperFACETS) project (award DE-SC0016605). JT is supported by the "Reducing Uncertainties in Biogeochemical Interactions through Synthesis and Computation (Reducing Uncertainties in Biogeochemical Interactions through Synthesis and Computation)" Scientific Focus Area. WR was supported by the Atmospheric System Research Program. This research used resources of the National Energy Research Scientific Computing Center, a Department of Energy Office of Science User Facility.

References

Albano, C. M., Dettinger, M. D., & Harpold, A. A. (2020). Patterns and drivers of atmospheric river precipitation and hydrologic impacts across the western United States. *Journal of Hydrometeorology*, *21*(1), 143–159. Retrieved from https://doi.org/10.1175/JHM-D-19-0119.1

Barnhart, T. B., Molotch, N. P., Livneh, B., Harpold, A. A., Knowles, J. F., & Schneider, D. (2016). Snowmelt rate dictates streamflow. *Geophysical Research Letters*, *43*(15), 8006–8016. Retrieved from https://doi.org/10.1002/2016GL069690

Bass, B., Rahimi, S., Goldenson, N., Hall, A., Norris, J., & Lebow, Z. J. (2023). Achieving realistic runoff in the western United States with a land surface model forced by dynamically downscaled meteorology. *Journal of Hydrometeorology*, *24*(2), 269–283. Retrieved from https://doi.org/10.1175/JHM-D-22-0047.1

Bowers, C., Serafin, K. A., & Baker, J. (2022). A performance-based approach to quantify atmospheric river flood risk. *Natural Hazards and Earth System Sciences*, *22*(4), 1371–1393. Retrieved from https://doi.org/10.5194/nhess-22-1371-2022

Bowers, C., Serafin, K. A., Tseng, K., & Baker, J. W. (2023). Atmospheric river sequences as indicators of hydrologic hazard in historical reanalysis and GFDL spear future climate projections. *Earth's Future*, *11*(12). Retrieved from https://doi.org/10.1029/2023EF003536

Cao, Q., Mehran, A., Ralph, F. M., & Lettenmaier, D. P. (2019). The role of hydrological initial conditions on atmospheric river floods in the Russian river basin. *Journal of Hydrometeorology*, *20*(8), 1667–1686. Retrieved from https://doi.org/10.1175/jhm-d-19-0030.1

Cayan, D. R., Dettinger, M. D., Kammerdiener, S. A., Caprio, J. M., & Peterson, D. H. (2001). Changes in the onset of spring in the western United States. *Bulletin of the American Meteorological Society*, *82*(3), 399–415. Retrieved from https://doi.org/10.1175/1520-0477(2001)082<0399:CITOOS>2.3.CO;2

Chen, X., & Leung, L. R. (2020). Response of landfalling atmospheric rivers on the U.S. west coast to local sea surface temperature perturbations. *Geophysical Research Letters*, *47*(18). Retrieved from https://doi.org/10.1029/2020GL089254

Chen, X., Leung, L. R., Gao, Y., Liu, Y., Wigmosta, M., & Richmond, M. (2018). Predictability of extreme precipitation in western U.S. watersheds based on atmospheric river occurrence, intensity, and duration. *Geophysical Research Letters*, *45*(21). Retrieved from https://doi.org/10.1029/2018GL079831

Chen, X., Leung, L. R., Wigmosta, M., & Richmond, M. (2019). Impact of atmospheric rivers on surface hydrological processes in western U.S. watersheds. *Journal of Geophysical Research: Atmospheres*, *124*(16), 8896–8916. Retrieved from https://doi.org/10.1029/2019JD030468

Copernicus Climate Change Service (C3S). (2017). ERA5: Fifth generation of ECMWF atmospheric reanalyses of the global climate [Dataset]. *Copernicus Climate Data Store (CDS)*. Retrieved from https://cds.climate.copernicus.eu/datasets/reanalysis-era5-pressure-levels?tab=overview

Corringham, T. W., McCarthy, J., Shulgina, T., Gershunov, A., Cayan, D. R., & Ralph, F. M. (2022). Climate change contributions to future atmospheric river flood damages in the western United States. *Scientific Reports*, *12*(1), 13747. Retrieved from https://doi.org/10.1038/s41598-022-15474-2

Dettinger, M. D. (2013). Atmospheric rivers as drought busters on the U.S. west coast. *Journal of Hydrometeorology*, *14*(6), 1721–1732. Retrieved from https://doi.org/10.1175/JHM-D-13-02.1

Dettinger, M. D., Ralph, F. M., Das, T., Neiman, P. J., & Cayan, D. R. (2011). Atmospheric rivers, floods and the water resources of California. *Water*, *3*(2), 445–478. Retrieved from https://doi.org/10.3390/w3020445

DeWalle, D. R., & Rango, A. (2008). In *Principles of snow hydrology* (pp. 146–181). Cambridge University Press. Retrieved from https://doi.org/10.1017/CBO9780511535673.007

Dominguez, F., Dall'erba, S., Huang, S., Avelino, A., Mehran, A., Hu, H., et al. (2018). Tracking an atmospheric river in a warmer climate: From water vapor to economic impacts. *Earth System Dynamics*, *9*(1), 249–266. Retrieved from https://doi.org/10.5194/esd-9-249-2018

Gonzales, K. R., Swain, D. L., Roop, H. A., & Diffenbaugh, N. S. (2022). Quantifying the relationship between atmospheric river origin conditions and landfall temperature. *Journal of Geophysical Research: Atmospheres*, *127*(20). Retrieved from https://doi.org/10.1029/2022JD037284

Guan, B., Molotch, N. P., Waliser, D. E., Fetzer, E. J., & Neiman, P. J. (2010). Extreme snowfall events linked to atmospheric rivers and surface air temperature via satellite measurements. *Geophysical Research Letters*, *37*(20). Retrieved from https://doi.org/10.1029/2010GL044696

Guan, B., & Waliser, D. E. (2015). Detection of atmospheric rivers: Evaluation and application of an algorithm for global studies. *Journal of Geophysical Research: Atmospheres*, *120*(24), 12514–12535. Retrieved from https://doi.org/10.1002/2015JD024257

Guo, Z. (2020). Estimating method of maximum infiltration depth and soil water supply. *Scientific Reports*, *10*(1), 9726. Retrieved from https://doi.org/10.1038/s41598-020-66859-0

Hardie, M. A., Cotching, W. E., Doyle, R. B., Holz, G., Lisson, S., & Mattern, K. (2011). Effect of antecedent soil moisture on preferential flow in a texture-contrast soil. *Journal of Hydrology*, *398*(3–4), 191–201. Retrieved from https://doi.org/10.1016/j.jhydrol.2010.12.008

Hastie, T., & Tibshirani, R. (1987). Generalized additive models: Some applications. *Journal of the American Statistical Association*, *82*(398), 371–386. Retrieved from https://doi.org/10.1080/01621459.1987.10478440

Henn, B., Musselman, K. N., Lestak, L., Ralph, F. M., & Molotch, N. P. (2020). Extreme runoff generation from atmospheric river driven snowmelt during the 2017 oroville dam spillways incident. *Geophysical Research Letters*, *47*(14). Retrieved from https://doi.org/10.1029/2020GL088189

Hersbach, H., Bell, B., Berrisford, P., Hirahara, S., Horányi, A., Muñoz-Sabater, J., et al. (2020). The era5 global reanalysis. *Quarterly Journal of the Royal Meteorological Society*, *146*(730), 1999–2049. Retrieved from https://doi.org/10.1002/qj.3803

Hou, G., & Chen, S. (2020). Probabilistic modeling of disrupted infrastructures due to fallen trees subjected to extreme winds in urban community. *Natural Hazards*, *102*(3), 1323–1350. Retrieved from https://doi.org/10.1007/s11069-020-03969-y

Hu, H., Dominguez, F., Kumar, P., McDonnell, J., & Gochis, D. (2018). A numerical water tracer model for understanding event-scale hydrometeorological phenomena. *Journal of Hydrometeorology*, *19*(6), 947–967. Retrieved from https://doi.org/10.1175/JHM-D-17-0202.1

Hu, J. M., & Nolin, A. W. (2019). Snowpack contributions and temperature characterization of landfalling atmospheric rivers in the western cordillera of the United States. *Geophysical Research Letters*, *46*(12), 6663–6672. Retrieved from https://doi.org/10.1029/2019GL083564

Jennings, K. S., Kittel, T. G. F., & Molotch, N. P. (2018). Observations and simulations of the seasonal evolution of snowpack cold content and its relation to snowmelt and the snowpack energy budget. *The Cryosphere*, *12*(5), 1595–1614. Retrieved from https://doi.org/10.5194/tc-12-1595-2018

Jones, K. A., Niknami, L. S., Buto, S. G., & Decker, D. (2022). Federal standards and procedures for the national watershed boundary dataset (wbd): Chapter 3 of section a, federal standards, book 11, collection and delineation of spatial data. Retrieved from https://doi.org/10.3133/tm11A3

Konrad, C. P., & Dettinger, M. D. (2017). Flood runoff in relation to water vapor transport by atmospheric rivers over the western United States, 1949–2015. *Geophysical Research Letters*, *44*(22). Retrieved from https://doi.org/10.1002/2017GL075399

Lavers, D. A., & Villarini, G. (2013). The nexus between atmospheric rivers and extreme precipitation across europe. *Geophysical Research Letters*, *40*(12), 3259–3264. Retrieved from https://doi.org/10.1002/grl.50636

Leung, L. R., & Qian, Y. (2009). Atmospheric rivers induced heavy precipitation and flooding in the western U.S. simulated by the wrf regional climate model. *Geophysical Research Letters*, *36*(3). Retrieved from https://doi.org/10.1029/2008gl036445

Li, D., Wrzesien, M. L., Durand, M., Adam, J., & Lettenmaier, D. P. (2017). How much runoff originates as snow in the western United States, and how will that change in the future. *Geophysical Research Letters*, *44*(12), 6163–6172. Retrieved from https://doi.org/10.1002/2017GL073551

Lora, J. M., Shields, C. A., & Rutz, J. J. (2020). Consensus and disagreement in atmospheric river detection: Artmip global catalogues. *Geophysical Research Letters*, *47*(20). Retrieved from https://doi.org/10.1029/2020gl089302

Marra, G., & Wood, S. N. (2011). Practical variable selection for generalized additive models. *Computational Statistics and Data Analysis*, *55*(7), 2372–2387. Retrieved from https://doi.org/10.1016/j.csda.2011.02.004

McCabe, G. J., Clark, M. P., & Hay, L. E. (2007). Rain-on-snow events in the western United States. *Bulletin of the American Meteorological Society*, *88*(3), 319–328. Retrieved from https://doi.org/10.1175/BAMS-88-3-319

Miller, D. H. (1977). Surface transports from ecosystems, chapter xvi. In *Water at the surface of the earth* (Vol. 21, pp. 423–473). Academic Press. Retrieved from https://doi.org/10.1016/S0074-6142(08)60494-5

Mundhenk, B. D., Barnes, E. A., & Maloney, E. D. (2016). All-season climatology and variability of atmospheric river frequencies over the north pacific. *Journal of Climate*, *29*(13), 4885–4903. Retrieved from https://doi.org/10.1175/Jcli-D-15-0655.1

Musselman, K. N., Lehner, F., Ikeda, K., Clark, M. P., Prein, A. F., Liu, C., et al. (2018). Projected increases and shifts in rain-on-snow flood risk over western north America. *Nature Climate Change*, *8*(9), 808–812. Retrieved from https://doi.org/10.1038/s41558-018-0236-4

O'Brien, T. A., Payne, A. E., Shields, C. A., Rutz, J., Brands, S., Castellano, C., et al. (2020). Detection uncertainty matters for understanding atmospheric rivers. *Bulletin of the American Meteorological Society*, *101*(6), E790–E796. Retrieved from https://doi.org/10.1175/bams-d-19-0348.1

Paltan, H., Waliser, D., Lim, W. H., Guan, B., Yamazaki, D., Pant, R., & Dadson, S. (2017). Global floods and water availability driven by atmospheric rivers. *Geophysical Research Letters*, *44*(20). Retrieved from https://doi.org/10.1002/2017GL074882

Pathiraja, S., Westra, S., & Sharma, A. (2012). Why continuous simulation? The role of antecedent moisture in design flood estimation. *Water Resources Research*, *48*(6). Retrieved from https://doi.org/10.1029/2011WR010997

Payne, A. E., Demory, M.-E., Leung, L. R., Ramos, A. M., Shields, C. A., Rutz, J. J., et al. (2020). Responses and impacts of atmospheric rivers to climate change. *Nature Reviews Earth amp; Environment*, *1*(3), 143–157. Retrieved from https://doi.org/10.1038/s43017-020-0030-5

Ralph, F. M., Coleman, T., Neiman, P. J., Zamora, R. J., & Dettinger, M. D. (2013). Observed impacts of duration and seasonality of atmospheric-river landfalls on soil moisture and runoff in coastal northern California. *Journal of Hydrometeorology*, *14*(2), 443–459. Retrieved from https://doi.org/10.1175/JHM-D-12-076.1

Ralph, F. M., & Dettinger, M. D. (2011). Storms, floods, and the science of atmospheric rivers. *Eos, Transactions American Geophysical Union*, *92*(32), 265–266. Retrieved from https://doi.org/10.1029/2011EO320001

Ralph, F. M., Neiman, P. J., & Rotunno, R. (2005). Dropsonde observations in low-level jets over the northeastern pacific ocean from caljet-1998 and pacjet-2001: Mean vertical-profile and atmospheric-river characteristics. *Monthly Weather Review*, *133*(4), 889–910. Retrieved from https://doi.org/10.1175/mwr2896.1

Ralph, F. M., Neiman, P. J., Wick, G. A., Gutman, S. I., Dettinger, M. D., Cayan, D. R., & White, A. B. (2006). Flooding on California's Russian river: Role of atmospheric rivers. *Geophysical Research Letters*, *33*(13). Retrieved from https://doi.org/10.1029/2006GL026689

Ralph, F. M., Rutz, J. J., Cordeira, J. M., Dettinger, M., Anderson, M., Reynolds, D., et al. (2019). A scale to characterize the strength and impacts of atmospheric rivers. *Bulletin of the American Meteorological Society*, *100*(2), 269–289. Retrieved from https://doi.org/10.1175/Bams-D-18-0023.1

R Core Team. (2023). R: A language and environment for statistical computing [Computer software manual]. *R Core Team* Retrieved from https://www.R-project.org/

Rhoades, A. M. (2023). ERA5 cold content [Dataset]. *NERSC*. Retrieved from https://portal.nersc.gov/archive/home/a/arhoades/Shared/www/ERA5_Cold_Content

Rhoades, A. M., Jones, A. D., Srivastava, A., Huang, H., O'Brien, T. A., Patricola, C. M., et al. (2020). The shifting scales of western U.S. landfalling atmospheric rivers under climate change. *Geophysical Research Letters*, *47*(17). Retrieved from https://doi.org/10.1029/2020GL089096

Rhoades, A. M., Risser, M. D., Stone, D. A., Wehner, M. F., & Jones, A. D. (2021). Implications of warming on western United States landfalling atmospheric rivers and their flood damages. *Weather and Climate Extremes*, *32*, 100326. Retrieved from https://doi.org/10.1016/j.wace.2021.100326

Rhoades, A. M., Zarzycki, C. M., Inda-Diaz, H. A., Ombadi, M., Pasquier, U., Srivastava, A., et al. (2023). Recreating the California new year's flood event of 1997 in a regionally refined earth system model. *Journal of Advances in Modeling Earth Systems*, *15*(10). Retrieved from https://doi.org/10.1029/2023MS003793

Rudisill, W., Flores, A., & McNamara, J. (2021). The impact of initial snow conditions on the numerical weather simulation of a northern rockies atmospheric river. *Journal of Hydrometeorology*, *22*(1), 155–167. Retrieved from https://doi.org/10.1175/JHM-D-20-0018.1

Rutz, J. J., Shields, C. A., Lora, J. M., Payne, A. E., Guan, B., Ullrich, P., et al. (2019). The atmospheric river tracking method intercomparison project (artmip): Quantifying uncertainties in atmospheric river climatology. *Journal of Geophysical Research: Atmospheres*, *124*(24), 13777–13802. Retrieved from https://doi.org/10.1029/2019jd030936

Rutz, J. J., Steenburgh, W. J., & Ralph, F. M. (2014). Climatological characteristics of atmospheric rivers and their inland penetration over the western United States. *Monthly Weather Review*, *142*(2), 905–921. Retrieved from https://doi.org/10.1175/Mwr-D-13-00168.1

Sharma, A., Wasko, C., & Lettenmaier, D. P. (2018). If precipitation extremes are increasing, why aren't floods? *Water Resources Research*, *54*(11), 8545–8551. Retrieved from https://doi.org/10.1029/2018WR023749

Shields, C. A., Rutz, J. J., Leung, L.-Y., Ralph, F. M., Wehner, M., Kawzenuk, B., et al. (2018). Atmospheric river tracking method intercomparison project (artmip): Project goals and experimental design. *Geoscientific Model Development*, *11*(6), 2455–2474. Retrieved from https://doi.org/10.5194/gmd-11-2455-2018

Siirila-Woodburn, E. R., Dennedy-Frank, P. J., Rhoades, A., Vahmani, P., Maina, F., Hatchett, B., et al. (2023). The role of atmospheric rivers on groundwater: Lessons learned from an extreme wet year. *Water Resources Research*, *59*(6). Retrieved from https://doi.org/10.1029/2022WR033061

Slinskey, E. A., Hall, A., Goldenson, N., Loikith, P. C., & Norris, J. (2023). Subseasonal clustering of atmospheric rivers over the western United States. *Journal of Geophysical Research: Atmospheres*, *128*(22). Retrieved from https://doi.org/10.1029/2023JD038833

Tao, J., & Barros, A. P. (2013). Prospects for flash flood forecasting in mountainous regions – An investigation of tropical storm fay in the southern appalachians. *Journal of Hydrology*, *506*, 69–89. Retrieved from https://doi.org/10.1016/j.jhydrol.2013.02.052

Tao, J., Wu, D., Gourley, J., Zhang, S. Q., Crow, W., Peters-Lidard, C., & Barros, A. P. (2016). Operational hydrological forecasting during the iphex-iop campaign – Meet the challenge. *Journal of Hydrology*, *541*, 434–456. Retrieved from https://doi.org/10.1016/j.jhydrol.2016.02.019

Ullrich, P. A., Zarzycki, C. M., McClenny, E. E., Pinheiro, M. C., Stansfield, A. M., & Reed, K. A. (2021). Tempestextremes v2.1: A community framework for feature detection, tracking, and analysis in large datasets. *Geoscientific Model Development*, *14*(8), 5023–5048. Retrieved from https://doi.org/10.5194/gmd-14-5023-2021

Waliser, D., & Guan, B. (2017). Extreme winds and precipitation during landfall of atmospheric rivers. *Nature Geoscience*, *10*(3), 179–183. Retrieved from https://doi.org/10.1038/ngeo2894

Wang, S., Ma, X., Zhou, S., Wu, L., Wang, H., Tang, Z., et al. (2023). Extreme atmospheric rivers in a warming climate. *Nature Communications*, *14*(1), 3219. Retrieved from https://doi.org/10.1038/s41467-023-38980-x

Wasko, C., Nathan, R., & Peel, M. C. (2020). Changes in antecedent soil moisture modulate flood seasonality in a changing climate. *Water Resources Research*, *56*(3). Retrieved from https://doi.org/10.1029/2019WR026300

Wood, S. N. (2010). Fast stable restricted maximum likelihood and marginal likelihood estimation of semiparametric generalized linear models. *Journal of the Royal Statistical Society - Series B: Statistical Methodology*, *73*(1), 3–36. Retrieved from https://doi.org/10.1111/j.1467-9868.2010.00749.x

Zhang, L., Zhao, Y., Cheng, T. F., & Lu, M. (2024). Future changes in global atmospheric rivers projected by cmip6 models. *Journal of Geophysical Research: Atmospheres*, *129*(3). Retrieved from https://doi.org/10.1029/2023JD039359

Zhou, Y., O'Brien, T. A., Ullrich, P. A., Collins, W. D., Patricola, C. M., & Rhoades, A. M. (2021). Uncertainties in atmospheric river lifecycles by detection algorithms: Climatology and variability. *Journal of Geophysical Research: Atmospheres*, *126*(8). Retrieved from https://doi.org/10.1029/2020jd033711

Zhou, Y., Wehner, M., & Collins, W. (2024). Back-to-back high category atmospheric river landfalls occur more often on the west coast of the United States. *Communications Earth & Environment*, *5*(1), 187. Retrieved from https://doi.org/10.1038/s43247-024-01368-w

Zhu, Y., & Newell, R. E. (1998). A proposed algorithm for moisture fluxes from atmospheric rivers. *Monthly Weather Review*, *126*(3), 725–735. Retrieved from https://doi.org/10.1175/1520-0493(1998)126<0725:apafmf>2.0.co;2